

## Chapter 2

# Fracture Behavior of IMCs at Cu/Pb-Free Solder Interface

### 2.1 Introduction

During the soldering process, the molten solder usually forms IMCs with the substrate material, which provides thermal, electrical, and mechanical integrity for the solder joint [1, 2]; therefore, it is necessary for the formation of high-quality solder joints. However, the IMCs are usually very brittle [3] and their thicknesses increase gradually when the solder joints generate heat during the service period; brittle fracture can easily occur in the IMCs and their strength can also get decreased [4–6]. So far, there have been many investigations trying to improve the reliability of the solder joints through decreasing the growth rate of the IMCs, but they can hardly eliminate the brittle fracture inside the IMC layer. With the decrease in size of the solder joints, the influence of IMC layer on the adhesive property of the solder joint is more significant, and the understanding of the fracture behavior of IMCs is more meaningful for evaluation of the reliability of the solder joints.

Because the IMC layers in the solder joints are usually very thin, it is difficult to carry out traditional mechanical property tests on the IMCs; the major method to test their mechanical property is the nanoindentation test, which can get the elastic modulus and hardness of the IMC [5–10], but cannot get their strength or evaluate their fracture behavior. Jiang et al. [11] reported a micropillar compression test to assess the mechanical properties of the IMCs, which is important because it is the first report describing the strength and fracture mechanisms of  $\text{Cu}_6\text{Sn}_5$ ; while fracture of the  $\text{Cu}_6\text{Sn}_5$  under compression loading is still a little bit different from the fracture in the service condition, the IMC grains in the real solder joints are usually elongated hemispherical or “scallop shaped”, and suffer the shear loading.

So far investigations on the fracture behavior of the IMC layers under external loadings are abundant, and some qualitative conclusions have been obtained. It was found that with increases in aging time and thickness of the IMC layer, the fracture transforms from a ductile fracture inside the solder into a cleavage fracture inside the IMC layer, and the joint strength decreases obviously [12–15]. However,

generally these investigations focus on the evolution of joint strength with increasing aging time rather than the fracture behavior of the IMCs. Besides, very few studies have investigated the influence of reflow time on the fracture behavior of the IMC layer and the solder joint. In fact, understandings on the influence of reflow time are more meaningful for finding proper soldering parameters, because the reflow time can be controlled to get the desired interfacial IMC thickness.

As the interfacial IMC layers are very thin ( $\sim 1\text{--}10\text{ }\mu\text{m}$ ) and located around the solder–substrate interface, when the solder joint is deformed by external loading, not only the loadings suffered by the solder can result in the fracture of IMC, but also the deformation of the substrate may also cause the fracture [16, 17]. Since the solder joints in the microelectronic devices serve in increasingly complex and dynamic environments, possibility of the fracture induced by deformation of the substrate is increasing, while the investigations on such cases are lack.

For the aforementioned reasons, in this chapter some new methods were designed to investigate the fracture behavior of the IMC layers induced by shear stress and deformation of the solder and the substrate, and the influencing factors on fracture behavior of the IMC layer are discussed. The research progress will be helpful for evaluating the reliability of the solder joints, and it is hoped that the proposed new test methods better reveal the property of the IMC layers.

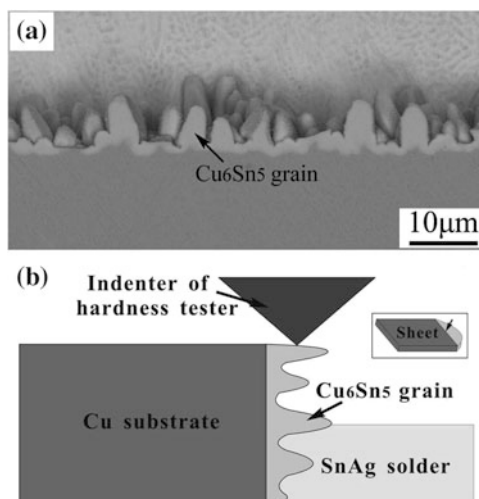
## 2.2 Experimental Procedure

### 2.2.1 *Indentation Test of Interfacial IMC Grains*

The substrate material used for the indentation test of the interfacial IMC grains is cold-drawn polycrystalline Cu with a purity of 99.99 % and a yield strength of about 300 MPa. The solder used in this study is Sn–4Ag solder alloy prepared by melting high-purity ( $>99.99\text{ }\%$ ) tin and silver at  $800\text{ }^{\circ}\text{C}$  for 30 min in vacuum. To prepare the test samples, a small block ( $5\text{ mm} \times 5\text{ mm} \times 5\text{ mm}$ ) was first spark cut from the Cu substrate, and then its side surface for reflowing was ground and carefully polished. After air drying, a soldering flux was dispersed on the polished area and a piece of solder alloy was stuck on it. The prepared samples were put in an oven with a temperature of  $260\text{ }^{\circ}\text{C}$  for 8 min after melting of the solder and then air cooled.

After the reflowing process, a thin sheet with a thickness of about 1.5 mm was sliced from the sample and its side surface was ground and carefully polished. To expose the  $\text{Cu}_6\text{Sn}_5$  grains, the superficial Sn–4Ag solder around the joint interface was removed by corrosion using the  $5\text{ }\%$  HCl +  $3\text{ }\%$   $\text{HNO}_3$  +  $\text{CH}_3\text{OH}$  (wt%) etching solution and the morphologies of the target  $\text{Cu}_6\text{Sn}_5$  grains were observed by a ZEISS Supra 35 scanning electron microscope (SEM), in order to make a morphological comparison of the indentation test. The morphology of the joint interface after corrosion is shown in Fig. 2.1a.

**Fig. 2.1** **a** Morphologies of the  $\text{Cu}_6\text{Sn}_5$  grains at the Sn–4Ag/Cu interface, **b** illustration on the shear test by Dynamic Ultramicroscopic Hardness tester. Reprinted from Ref. [18]. Copyright 2011, with permission from AIP Publishing LLC



The DUH-211 Dynamic Ultramicroscopic Hardness tester was employed to conduct the indentation tests, because it is easily operated and can record the dynamic load–depth relationships. The indenter is a triangular pyramid and the indentation location is the center portion of the target  $\text{Cu}_6\text{Sn}_5$  grains, as illustrated in Fig. 2.1b. The load was chosen to be 20 mN and the loading speed was set to be 1.90 mN/s. The force–depth relationships were recorded. After the indentation tests, the front views of the target  $\text{Cu}_6\text{Sn}_5$  grains were first observed, the cracked  $\text{Cu}_6\text{Sn}_5$  fragments were flushed away by ultrasonic cleaning, and then the fracture surface of the target grains was also observed by SEM.

## 2.2.2 Fracture of IMCs Induced by Deformation of Solder

The substrate material used for the in situ observation of the fracture behavior of the interfacial IMCs induced by deformation of the solder is also cold-drawn polycrystalline Cu, and the solder is the Sn–4Ag (wt%) alloy. The sample preparation process for interfacial observation is similar to the process mentioned in Sect. 2.2.1, as in Fig. 2.2a. The prepared samples were put in an oven with a temperature of 260  $^{\circ}\text{C}$ , for 1, 3, or 8 min; the molten solder is then taken out and quenched with alcohol. After the reflow process, the overlaid solders on the samples were eroded with the 5 % HCl + 3 %  $\text{HNO}_3$  +  $\text{CH}_3\text{OH}$  (wt%) etching solution to expose the  $\text{Cu}_6\text{Sn}_5$  grains. The morphologies of the  $\text{Cu}_6\text{Sn}_5$  layers were observed by a ZEISS Supra 35 SEM and a LEXT OLS4000 measuring laser confocal microscope and their roughnesses were measured directly using the latter. The contours of the interfacial IMC layers were analyzed using the SISC IAS V8.0 software to obtain their thickness.

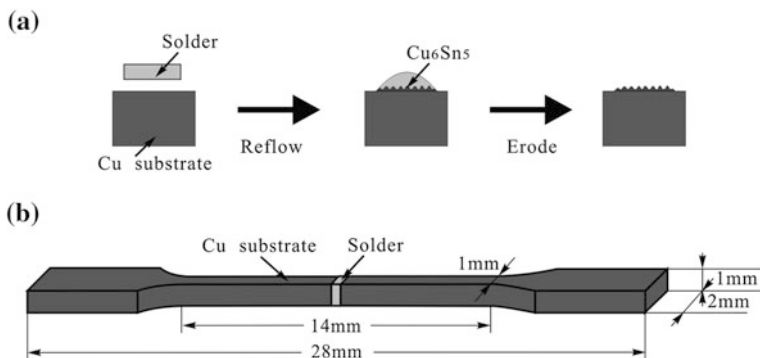


**Fig. 2.2** **a** Preparing process of samples for interfacial IMC morphology observation, **b** shape and dimension of the tensile samples. Reprinted from Ref. [19]. Copyright 2012, with permission from AIP Publishing LLC

To prepare the tensile samples, the Cu substrates were first spark cut into blocks with a dog-bone-shaped side cross section; the blocks were then spark cut at their midst and the surfaces for reflow were ground and electrolytically polished. A flux was dispersed on the polished surfaces of the blocks before reflow, then the Sn–4Ag sheets were sandwiched between them, and finally two graphite plates were clamped on the sides to avoid outflow of the molten solder. The reflow processes are the same to those mentioned above. Then the prepared samples were sliced into standard tensile specimens, their side surfaces were ground with 2000# SiC abrasive paper, and carefully polished with 1- $\mu\text{m}$  diamond powder. The shape and dimension of the final prepared specimens are presented in Fig. 2.2b.

The tensile tests were carried out by Gatan MTEST2000ES tensile stage installed on the ZEISS Supra 35 SEM. The motor speeds were set as 0.033, 0.1, and 0.4  $\text{mm min}^{-1}$ , respectively. Since the Cu substrate only shows very slight elastic deformation, the strain rate was approximately calculated by dividing the cross-beam speed with the thickness of the solder in the solder joints ( $\sim 0.5 \text{ mm}$ ), thus the strain rates are estimated to be about  $1.1 \times 10^{-3} \text{ s}^{-1}$ ,  $3.3 \times 10^{-3} \text{ s}^{-1}$  and  $1.33 \times 10^{-2} \text{ s}^{-1}$ , respectively. Three samples were tested under each condition and the tensile strength is their average value. The interfacial fracture morphologies of selected solder joints were observed at certain strains, and the fracture surfaces were also observed by SEM after the tests to comprehensively reveal the fracture mechanisms.

### 2.2.3 Fracture of IMCs Induced by Deformation of Substrate

Two kinds of Cu substrates were used in the study of fracture behavior of IMCs induced by deformation of the substrate. The first is the cold-drawn

oxygen-free-high-conductivity (OFHC) Cu with a yield strength of about 300 MPa. The second one is Cu crystal composed of centimeter-sized grains with a yield strength of about 32 MPa. Since the coarse grains are close to the prepared specimens in size, the latter can be approximately regarded as single crystals. The solder used in this study is also the Sn–4Ag (wt%) alloy.

To prepare the test specimens, the Cu substrates were first spark cut into blocks with a side section of dog-bone shape, and then the surfaces for soldering were ground and electrolytically polished. After air drying, a soldering flux was dispersed on the polished area, and a thin solder sheet was stick on it. The prepared samples were put in an oven with a temperature of 260 °C, kept for 8 min after melting of the solder, and then cooled down in air. As the fracture behaviors of the IMC layer are affected by its thickness, some samples were aged at 180 °C for 4 days to get thicker IMC layer. After the reflow and aging processes, the prepared samples were sliced into test specimens and then their side surfaces were ground and carefully polished for interfacial observations. The preparing process and dimension of the test specimens are presented in Fig. 2.3. For the specimens in this study, the IMC layers are driven to deform by the Cu substrate and the solder is unconstrained, in order to make sure that the solder has little influence on fracture of the IMC layers.

All the tests were carried out by the Gatan MTEST2000ES Tensile Stage equipped on the ZEISS Supra 35 SEM, and the crossbeam speed was set as  $0.033 \text{ mm min}^{-1}$ . To reveal the fracture behaviors of the IMC layers, the tests were paused at some displacements and the interfacial morphologies were observed. As there is no strain gauge on the tensile stage, the macroscopic images comprising the observation region were taken for calculating the strain. The local displacements ( $\Delta l$ ) in the macroscopic images were obtained through measuring the distances between the reference points and comparing them with the original distance ( $l_0$ ), and the local strains were calculated by dividing the displacement with the original distance. The total displacement ( $\Delta L$ ) was recorded by the tensile stage, and the

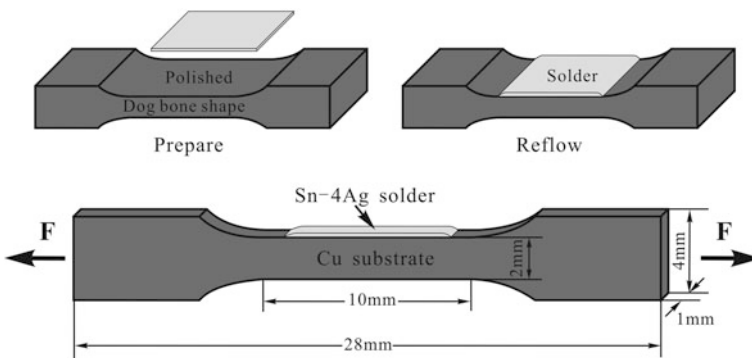


**Fig. 2.3** Preparing processes and dimension of the test specimens for observation on fracture behavior of interfacial IMC layers induced by deformation of the substrate. Reprinted from Ref. [20]. Copyright 2011, with permission from Elsevier

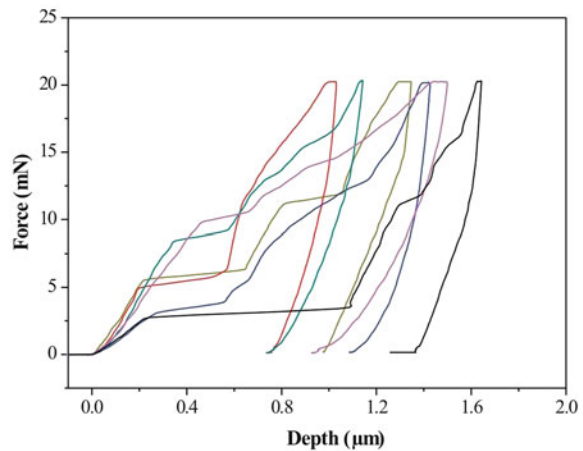
equivalent “gauge length” ( $L_0$ ) was estimated by the equation:  $L_0 = l_0 \Delta L / \Delta l$ . Based on that, the strain in the stress–strain curves was calculated by dividing  $\Delta L$  with the mean value of  $L_0$  obtained at different displacements. After the tests, the overlaid solders on the specimens were removed by eroding with a solution composed of 5 % hydrochloric acid, 3 % nitric acid, and 92 % methanol, and the morphologies of the fractured IMC grains were also observed by SEM.

### 2.3 Shear Fracture Behavior and Strength of $\text{Cu}_6\text{Sn}_5$ Grains

A group of force–depth curves of the indentation tests are shown in Fig. 2.4; the depth in the figure is actually the shear displacement of the  $\text{Cu}_6\text{Sn}_5$  grains. As in the figure, though the loadings are 20 mN for all the tests, the displacements are quite different because the  $\text{Cu}_6\text{Sn}_5$  grains are different in size and shape. Nevertheless, there are similarities in all the curves. Within each curve, the depth increases approximately linear with increasing force during the initial deforming process. When the force increases to a certain value, a depth burst occurs which may correspond to the fracture in the  $\text{Cu}_6\text{Sn}_5$  grain [13]. Besides, similar bursts have been observed when the  $\text{Cu}_6\text{Sn}_5$  micropillar fracture under compression loadings by cleavage [11]. After the burst, the depth again increases with increasing force and the slope is similar to the initial stage. For some curves, there are secondary bursts. As the bursts on different curves are quite different, the fracture morphologies of the correlating  $\text{Cu}_6\text{Sn}_5$  grains were observed to reveal the differences.

Figures 2.5 and 2.6 show the morphologies of two representative  $\text{Cu}_6\text{Sn}_5$  grains before and after the indentation tests. The morphologies of a  $\text{Cu}_6\text{Sn}_5$  grain fractured at a low force are shown in Fig. 2.5. Figure 2.5a exhibits the target  $\text{Cu}_6\text{Sn}_5$  grain before the indentation test, which is bamboo shoot-like in shape and the length is

**Fig. 2.4** Force–depth curves of the shear tests. Reprinted from Ref. [18]. Copyright 2011, with permission from AIP Publishing LLC



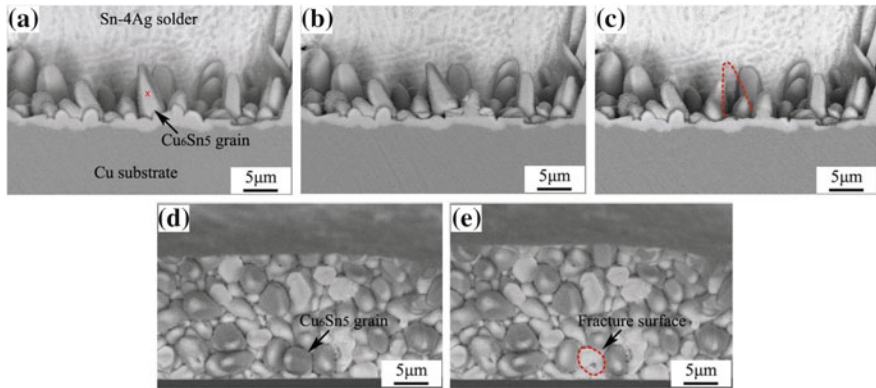


**Fig. 2.5** Morphologies of a  $\text{Cu}_6\text{Sn}_5$  grain fractured at the foundation: *front views* **a** before indentation test, **b** after indentation test, and **c** after ultrasonic cleaning; *top views* **d** before indentation test and **e** after ultrasonic cleaning. Reprinted from Ref. [18]. Copyright 2011, with permission from AIP Publishing LLC

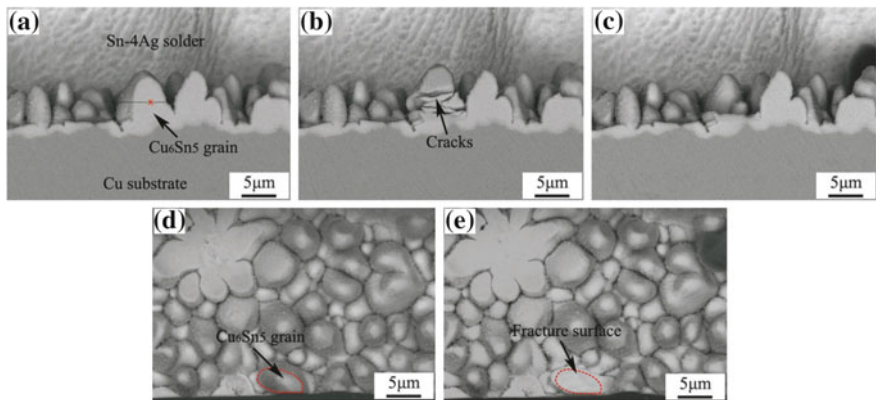


**Fig. 2.6** Morphologies of a  $\text{Cu}_6\text{Sn}_5$  grain fractured at the center portion: *front views* **a** before indentation test, **b** after indentation test, and **c** after ultrasonic cleaning; *top views* **d** before indentation test and **e** after ultrasonic cleaning. Reprinted from Ref. [18]. Copyright 2011, with permission from AIP Publishing LLC

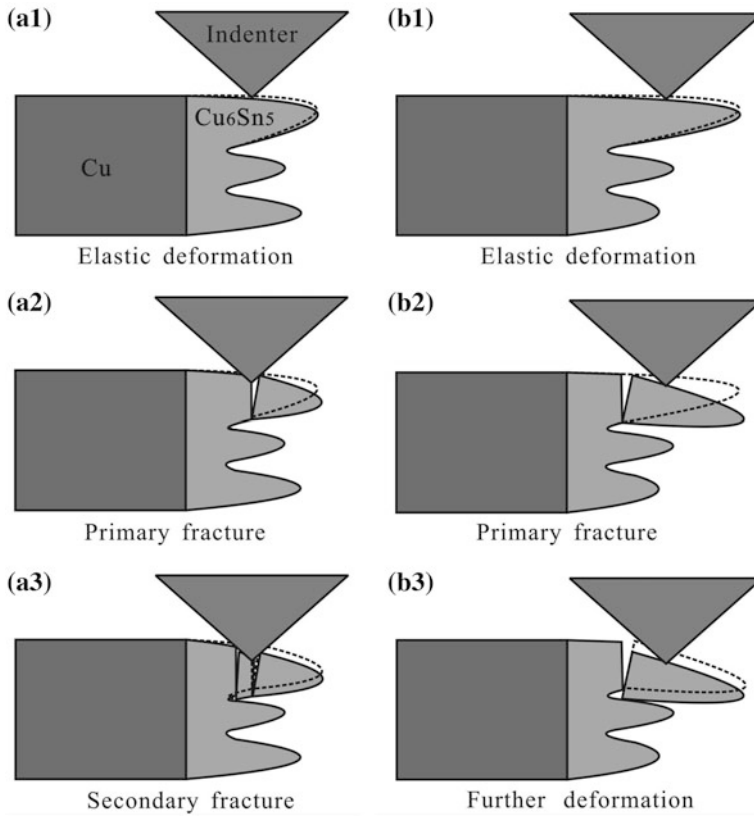
about  $10\ \mu\text{m}$ ; the indentation location is indicated by a red “X”. After the test, the target  $\text{Cu}_6\text{Sn}_5$  grain only exhibited a little tilt compared with the initial state, while the surrounding little  $\text{Cu}_6\text{Sn}_5$  grains were broken (see Fig. 2.5b). Figure 2.5c shows the front view after the ultrasonic cleaning. The target  $\text{Cu}_6\text{Sn}_5$  was washed away, indicating that actually it has fractured at the foundation under the indentation test. The top views of the target  $\text{Cu}_6\text{Sn}_5$  grain are presented in Fig. 2.5d, e, respectively. By comparing them, the fracture surface of the target  $\text{Cu}_6\text{Sn}_5$  grain can be determined easily, as indicated by the red circle.



Figure 2.6 shows the morphologies of a  $\text{Cu}_6\text{Sn}_5$  grain fractured at a higher force. The front view of the target grain before the test is shown in Fig. 2.6a. As in the figure, the target grain is a little bit podgy compared with that in Fig. 2.5a, and the indentation location is also indicated by the red “X”. After the indentation test, it is interesting to find that there are some parallel cracks in the target  $\text{Cu}_6\text{Sn}_5$  grain, but there is no breakage in the surrounding  $\text{Cu}_6\text{Sn}_5$  grains (see Fig. 2.6b). According to the width and location of the cracks, the cracking at the center portion of the grain is predicated to be formed initially, i.e. it is the primary fracture corresponding to the first depth burst in the curve, and the other cracks were formed in the further indentation process. Based on the predication, the primary fracture location is lined out in Fig. 2.6a, and it is notable that the primary fracture occurs at the indentation location. After the ultrasonic cleaning, the cracked  $\text{Cu}_6\text{Sn}_5$  fragments were washed away, as in Fig. 2.6c, but the surrounding  $\text{Cu}_6\text{Sn}_5$  grains still show no breakage. Figure 2.6d, e show the top views of the target grain before and after the test. Although the primary fracture surface is not the fracture surface in Fig. 2.6e, it can be determined by comparing the front view and the top view of the target  $\text{Cu}_6\text{Sn}_5$  grain based on a charting principle. After determining the fracture surfaces, their areas can be measured and the fracture strength of the  $\text{Cu}_6\text{Sn}_5$  grains can be calculated.

Based on the foresaid discussions on the indentation curves and the fracture morphologies, the fracture processes of the two fracture modes are illustrated in Fig. 2.7. In all the figures, the contours of the  $\text{Cu}_6\text{Sn}_5$  grains at the last stage are presented with the broken lines to clearly show the fracture process. Figure 2.7a1–a3 show the fracture process of the  $\text{Cu}_6\text{Sn}_5$  grain shown in Fig. 2.6. During the initial deforming stage, the  $\text{Cu}_6\text{Sn}_5$  grain deforms elastically, as in Fig. 2.7a1. When the load increases to a critical value, the  $\text{Cu}_6\text{Sn}_5$  grain fractures at its center portion (see Fig. 2.7a2), inducing the first depth burst on the force–depth curve. As the fracture location is very close to the indentation location, the flexural torque on the fracture plane is little and the fracture should be induced by the shear stress. In the latter process, the indenter is sustained by the residual part of the target  $\text{Cu}_6\text{Sn}_5$  grain, as shown in Fig. 2.7a3; some parallel secondary cracks are formed, while the surrounding  $\text{Cu}_6\text{Sn}_5$  grains are not broken. The fracture process of the  $\text{Cu}_6\text{Sn}_5$  grain in Fig. 2.5 is illustrated in Fig. 2.7b1–b3. As in the figures, the  $\text{Cu}_6\text{Sn}_5$  grain also only displays elastic deformation at the first stage, but fractures at its foundation when the load increases to a certain value. Because there is an arm of force between the fracture location and the indentation location, the  $\text{Cu}_6\text{Sn}_5$  grain fractures like a cantilever; i.e., it is the flexural torque that causes the fracture, and the fracture occurs at the foundation because the flexural torque there is the highest. The depth burst in this fracture mode is much higher than the first fracture mode, because the indenter should descend a larger distance until it can be sustained by the  $\text{Cu}_6\text{Sn}_5$  grains around the target grain. As a result, the secondary fracture occurs in the surrounding  $\text{Cu}_6\text{Sn}_5$  grains rather than in the residual part of the target  $\text{Cu}_6\text{Sn}_5$  grain. It is predicated that the slender  $\text{Cu}_6\text{Sn}_5$  grains are more likely to fracture at the foundation at a lower stress, while the podgy grains tend to fracture at the center portion at a higher stress. It has been widely accepted that the fracture



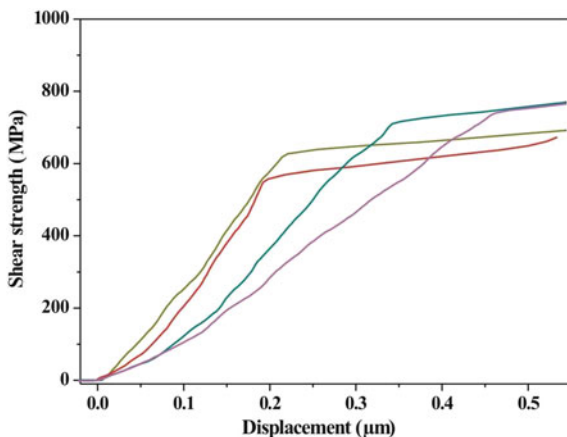


**Fig. 2.7** Illustrations on fracture processes of  $\text{Cu}_6\text{Sn}_5$  grains fractured **a1–a3** at the center portion and **b1–b3** at the foundation. Reprinted from Ref. [18]. Copyright 2011, with permission from AIP Publishing LLC

behavior of the IMCs layer is affected by their thickness and morphologies, the present work provides a strong and direct support for that.

As discussed above, the primary fracture at the center portion is induced by the shear stress; therefore, the fracture strength in this condition can be considered similar to the shear strength of the  $\text{Cu}_6\text{Sn}_5$  grains. After measuring the fracture surfaces of the  $\text{Cu}_6\text{Sn}_5$  grains, the shear stresses were calculated by dividing the force with the fracture area. Figure 2.8 shows the first stage of the strength–displacement curves of a few  $\text{Cu}_6\text{Sn}_5$  grains fractured at their center portion, in which the bursts occur at the stresses as high as about 670 MPa. Since the bursts correspond to the primary shear fractures in the  $\text{Cu}_6\text{Sn}_5$  grains, the shear fracture strength of  $\text{Cu}_6\text{Sn}_5$  is easily estimated to be around 670 MPa. This is the first report on the shear fracture strength of the  $\text{Cu}_6\text{Sn}_5$  intermetallic compounds. Jiang et al. [11] have reported that the  $\text{Cu}_6\text{Sn}_5$  micropillar fractures along certain crystallographic planes under compressive loadings, the fracture stress was around

**Fig. 2.8** The first stage of shear stress–displacement curves of the  $\text{Cu}_6\text{Sn}_5$  grains fractured at their center portion. Reprinted from Ref. [18]. Copyright 2011, with permission from AIP Publishing LLC



1356 MPa and the angle between the compressive direction and the fracture plane is about  $60^\circ$ . Based on that, the shear fracture stress at the fracture plane is estimated to be about 587 MPa through dividing the shear component of the compressive stress by the area of the fracture plane, which is close to the current results.

It is widely known that with the decreasing trend in size of the solder joints, the solder joints will contain fewer  $\text{Cu}_6\text{Sn}_5$  grains, makes the fracture behaviors of the  $\text{Cu}_6\text{Sn}_5$  grains more influential on the strength of the solder joints [21–23]. Therefore, the results on the shear strength of the  $\text{Cu}_6\text{Sn}_5$  grains will be very important for evaluating the reliability of the solder joints. In addition, as the indentation test in this study is easy to carry out, it is expected that this experimental method can be popularized in investigation of the fracture strengths of the IMCs.

## 2.4 Fracture Behavior of $\text{Cu}_6\text{Sn}_5$ Induced by Deformation of Solder

### 2.4.1 Growth Behavior of $\text{Cu}_6\text{Sn}_5$ at Sn–4Ag/Cu Interface

The microstructures of the Sn–4Ag/Cu joint interfaces reflowed for different times and morphologies of the corresponding interfacial IMC grains are shown in Fig. 2.9. Figure 2.9a presents the interface reflowed for 1 min, in which the interfacial IMC layer is very thin, and was confirmed to be pure  $\text{Cu}_6\text{Sn}_5$  by energy dispersive spectroscopy (EDS). In the corresponding images of the  $\text{Cu}_6\text{Sn}_5$  grains shown in Fig. 2.9b, it can be found that their sizes are around 1–2  $\mu\text{m}$ . For the solder joint reflowed for 3 min, the interfacial IMC layer is obviously thicker (see Fig. 2.9c), and it is still pure  $\text{Cu}_6\text{Sn}_5$ . Meanwhile, the sizes of the  $\text{Cu}_6\text{Sn}_5$  grains become a little bit different, as in Fig. 2.9d, the grain size is in the range of 1–4  $\mu\text{m}$ . After reflowed for 8 min, the IMC layer becomes much thicker, and their grain size is in the range of

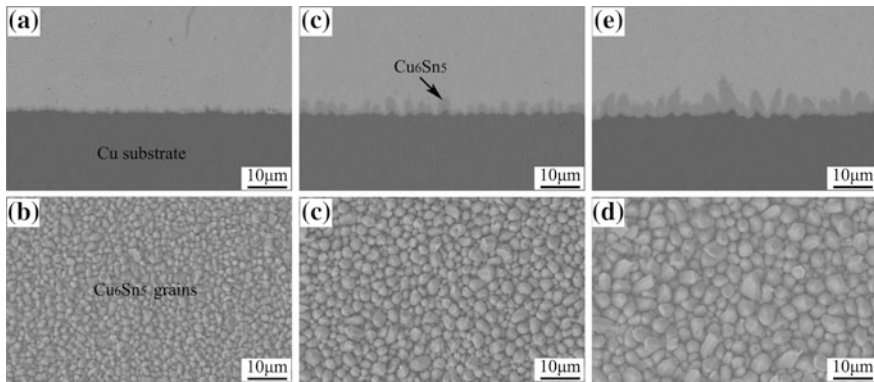


**Fig. 2.9** Interfacial microstructure and morphologies of  $\text{Cu}_6\text{Sn}_5$  grains at the Sn–4Ag/Cu interface reflowed for **a** and **b** 1 min, **c** and **d** 3 min, **e** and **f** 8 min. Reprinted from Ref. [19]. Copyright 2012, with permission from AIP Publishing LLC

2–6  $\mu\text{m}$  (see Fig. 2.9e, f), implying that the difference in grain size becomes more serious with increasing reflow time. Thermodynamically, there should be a  $\text{Cu}_3\text{Sn}$  layer between the Cu and  $\text{Cu}_6\text{Sn}_5$ , but the  $\text{Cu}_3\text{Sn}$  layer is usually very thin after reflow, because its formation requires extended contact times [3, 24]. Since the SEM cannot reveal the three-dimensional (3D) morphologies of the  $\text{Cu}_6\text{Sn}_5$  grains, the measuring laser confocal microscope was employed to observe the 3D morphologies of the  $\text{Cu}_6\text{Sn}_5$  grains, in order to reveal their shape more visually.

The 3D morphologies of the  $\text{Cu}_6\text{Sn}_5$  layers in Fig. 2.9 are shown in Fig. 2.10. At the joint interface reflowed for 1 min, the  $\text{Cu}_6\text{Sn}_5$  layer is very flat, as in Fig. 2.10a, few prominent  $\text{Cu}_6\text{Sn}_5$  grains can be observed. Figure 2.10b shows the  $\text{Cu}_6\text{Sn}_5$  grains reflowed for 3 min, it is notable that the  $\text{Cu}_6\text{Sn}_5$  layer becomes much coarser, the grain size is much larger and some protrudent  $\text{Cu}_6\text{Sn}_5$  grains appear, which may be attributed to the difference in growth rates of the  $\text{Cu}_6\text{Sn}_5$  grains with different orientations [3, 25]. After reflowed for 8 min, the increases in grain size and surface roughness of the  $\text{Cu}_6\text{Sn}_5$  layer are more obvious, and there are much more protrudent  $\text{Cu}_6\text{Sn}_5$  grains (see Fig. 2.10c). The images in Fig. 2.9a, c, e are actually cross sections of these  $\text{Cu}_6\text{Sn}_5$  layers, thus they consist well with the 3D images.

To analyze the stress applied on the  $\text{Cu}_6\text{Sn}_5$  grains and their fracture behavior, it is necessary to give a quantitative description on their shape. According to Figs. 2.9 and 2.10, the protrudent  $\text{Cu}_6\text{Sn}_5$  grains are centrosymmetric grains with the contour lines of their cross sections similar to the parabola; thus in this study, they are approximately described by a revolution body of the parabola  $y = ax^2$ , in which  $y$  is the length of the  $\text{Cu}_6\text{Sn}_5$  grain,  $x$  is the radius and  $a$  is a shape parameter. The underside radius of the  $\text{Cu}_6\text{Sn}_5$  grain is defined as  $r$ . Since fracture of the  $\text{Cu}_6\text{Sn}_5$  layer usually occurs in the protrudent  $\text{Cu}_6\text{Sn}_5$  grains, the length and underside radius of the five largest  $\text{Cu}_6\text{Sn}_5$  grains in Fig. 2.9a, c, e were measured, the average sizes are obtained as below, respectively:

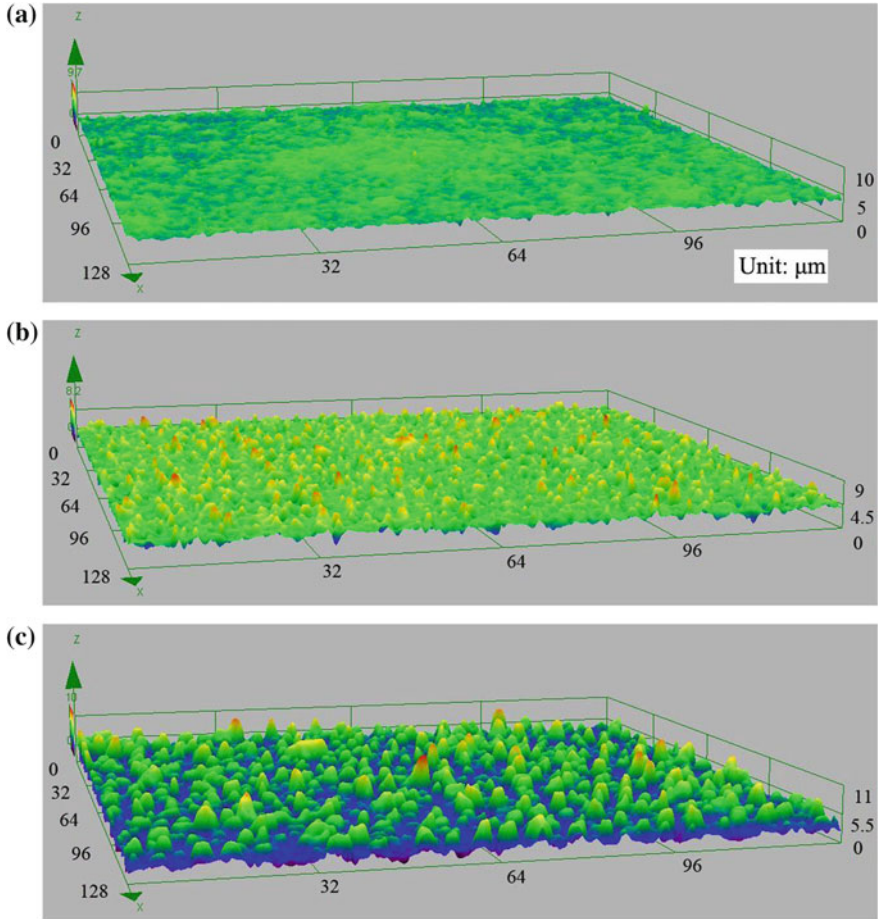


**Fig. 2.10** Three-dimensional images of  $\text{Cu}_6\text{Sn}_5$  grains at the Sn-4Ag/Cu interface reflowed for **a** 1 min, **b** 3 min and **c** 8 min. Reprinted from ref. [19], Copyright 2012, with permission from AIP Publishing LLC

$$\begin{aligned}
 l_{1\min} &= 1.52 \mu\text{m}, & r_{1\min} &= 1.1 \mu\text{m} \\
 l_{3\min} &= 3.84 \mu\text{m}, & r_{3\min} &= 1.67 \mu\text{m} \\
 l_{8\min} &= 6.41 \mu\text{m}, & r_{8\min} &= 1.92 \mu\text{m}
 \end{aligned}$$

According to the underside radius and length of the  $\text{Cu}_6\text{Sn}_5$  grains, their shape parameters were calculated to be  $a_{1\min} = 1.26$ ,  $a_{3\min} = 1.37$ ,  $a_{8\min} = 1.74$ , respectively. In consequence, the shape of the  $\text{Cu}_6\text{Sn}_5$  grains can be described quantitatively. The stress applied on the  $\text{Cu}_6\text{Sn}_5$  grains will be analyzed later to express the fracture behaviors of the latter.

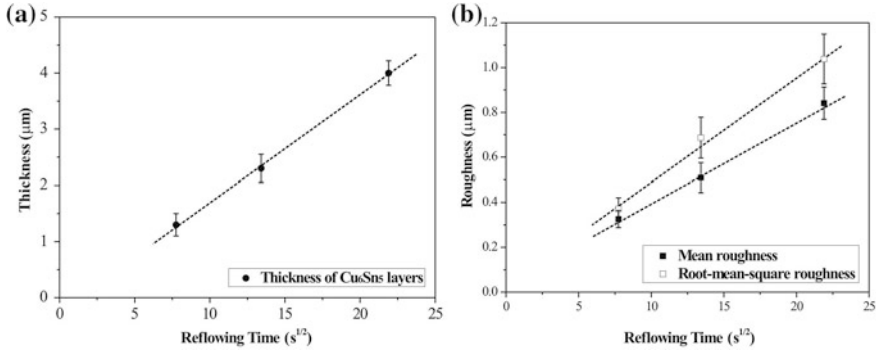


**Fig. 2.11** **a** Interfacial Cu<sub>6</sub>Sn<sub>5</sub> thickness–reflow time relationship, **b** roughness–reflow time relationship. Reprinted from Ref. [19]. Copyright 2012, with permission from AIP Publishing LLC

Figure 2.11 shows the average thickness of the Cu<sub>6</sub>Sn<sub>5</sub> layers and the roughness of the solder/Cu<sub>6</sub>Sn<sub>5</sub> interfaces at different solder joints. As in Fig. 2.11a, the thickness of the Cu<sub>6</sub>Sn<sub>5</sub> layers increase linearly with increasing square root of the reflow time. It is about 1.2 μm at the interface reflowed for 1 min, 2.4 μm at the interface reflowed for 3 min, and 4 μm at that reflowed for 8 min. As the thicknesses of the Cu<sub>6</sub>Sn<sub>5</sub> layers are close to their grain sizes, it can be confirmed that the Cu<sub>6</sub>Sn<sub>5</sub> layer is a single layer of grains. Since the surface roughness of the Cu<sub>6</sub>Sn<sub>5</sub> layer is a reflection of the protrudent segment of the Cu<sub>6</sub>Sn<sub>5</sub> grains, they may affect the fracture behavior of the latter. Therefore, the roughness of the Cu<sub>6</sub>Sn<sub>5</sub> layers were measured by measuring laser confocal microscope, both the root-mean-square roughness and the mean roughness were exported. As in Fig. 2.11b, the two roughness parameters also increase approximately linear with increasing square root of the reflow time, and their difference increases with increasing reflow time, induced by the greater difference in size of Cu<sub>6</sub>Sn<sub>5</sub> grains at the long-term reflowed joint interface. Since the mean roughness equals to half of the average distance between the peaks and bottoms of the surface of the Cu<sub>6</sub>Sn<sub>5</sub> layer, the average protrudent length of the Cu<sub>6</sub>Sn<sub>5</sub> grains is about 1.6 μm, and that of the protrudent Cu<sub>6</sub>Sn<sub>5</sub> grains can be twice as longer as that length. The differences in thickness and morphologies of the interfacial Cu<sub>6</sub>Sn<sub>5</sub> grains may affect the stress applied on them and in turn their fracture behaviors.

### 2.4.2 Fracture Behavior at Sn–4Ag/Cu Interface

The tensile stress–strain curves and strength of the solder joints are shown in Fig. 2.12. Figure 2.12a shows the stress–strain curves of the solder joint reflowed for 3 min and tested at three different strain rates. The strains were calculated by first subtracting the elastic displacement of the Cu substrate from the total displacement, and then divided the result with the thickness of the solder in the solder

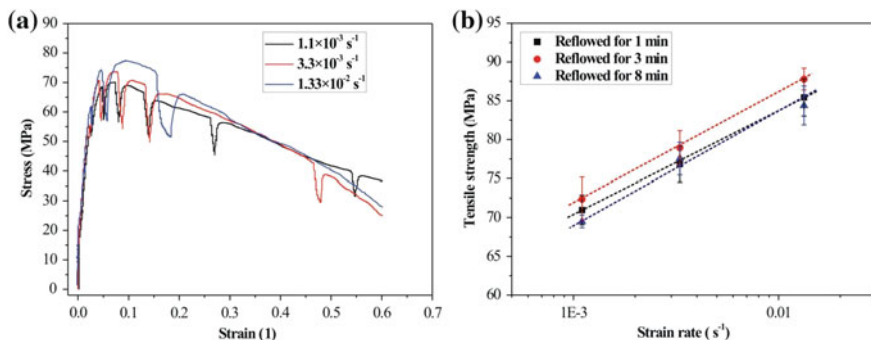


**Fig. 2.12** Tensile behaviors of Sn-4Ag/Cu solder joints: **a** tensile stress–strain curves of the solder joint reflowed for 3 min; and **b** tensile strengths at three different strain rates. Reprinted from Ref. [19]. Copyright 2012, with permission from AIP Publishing LLC

joints. Therefore, the tensile curves of the solder joints are very similar to the tensile curves of the solder alloys [26, 27], the stress decreases shortly after yielding of the solder, and also the elongation is very high. The three curves have similar styles and approximately coincident elastic stages, the tensile strength (UTS) at higher strain rate is a little higher, and the corresponding strain to the UTS is around 0.06–0.08. During the holding period, obvious stress relaxation occurred. Since the Sn–Ag solder has superior ductility, the solder joints fracture at very high strain. Different from the pure solder sample, not only necking of the solder but also local fracture in the joint interface can induce the decrease in stress of the solder joint.

The average UTSs of the solder joints tested at different strain rates are exhibited in Fig. 2.12b. As in the figure, the UTS of the solder joints reflowed for the same time increase with increasing strain rate, and the UTS of the solder joints reflowed 3 min is higher than the other two groups, albeit only a little. Since the solders in all the solder joints are the same, the difference in UTSs of the solder joint reflowed for different times can only be resulted from their different interfacial microstructures. Besides, the UTSs of solder joints also show exponential increase with increasing strain rate, which is similar to the relationship between the strain rate and yield strength of the solder alloy [27, 28]. The influencing mechanisms of strain rate and reflow time will be discussed later in detail.

To reveal the interfacial fracture mechanisms, fracture processes of the solder joints were in situ observed. Figure 2.13 shows the interfacial fracture processes of the solder joints reflowed for 1 min and tested at the strain rate of  $1.33 \times 10^{-2}$ , with the strains labeled in each figure. At the early stage of the tensile process, the deformation is slight and only visible around the joint interface. As in Fig. 2.13a, a deformation step was formed at the  $\text{Cu}_6\text{Sn}_5$ /solder interface, which was induced by deformation mismatch between the solder and the Cu substrate. With increasing strain, the interfacial deformation becomes obvious, and serious strain concentration occurs inside the solder close to the joint interface (see Fig. 2.13b). As a result, the interfacial damage develops very fast, resulting in the initiation of some



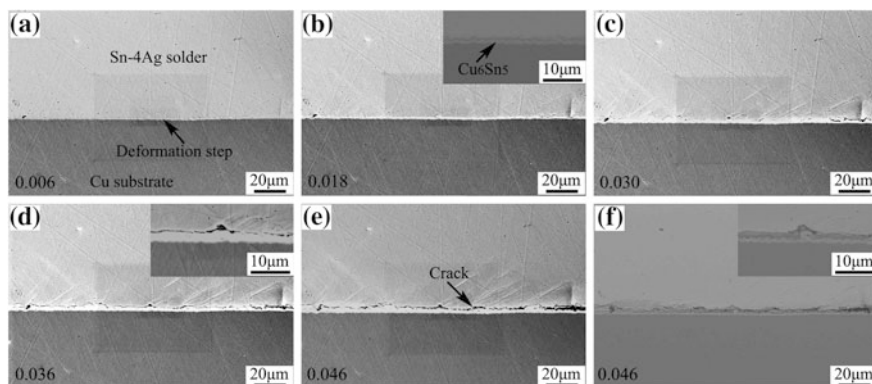


**Fig. 2.13** Interfacial fracture morphologies of Sn-4Ag/Cu solder joints reflowed for 1 min and tested at the strain rate of  $1.33 \times 10^{-2} \text{ s}^{-1}$ . Reprinted from Ref. [19]. Copyright 2012, with permission from AIP Publishing LLC

microcracks at the interface, as in Fig. 2.13c. In the further deformation process, the microcracks become wider and gradually connect with each other, inducing the interfacial fracture, as in Fig. 2.13d, e. In the backscattered electron image (Fig. 2.13f), it can be found that fracture occurs in the solder around the  $\text{Cu}_6\text{Sn}_5$ /solder interface, and there is no cracking in the  $\text{Cu}_6\text{Sn}_5$  layers. For the joint interface reflowed for 1 min, the strain concentration zone is thin and the interfacial fracture occurs at a low strain.

The interfacial fracture process of the solder joints reflowed for 3 min and tested at two different strain rates are exhibited in Fig. 2.14; the stains were also labeled in the figures. Figure 2.14a–c show the interfacial fracture process of the solder joints

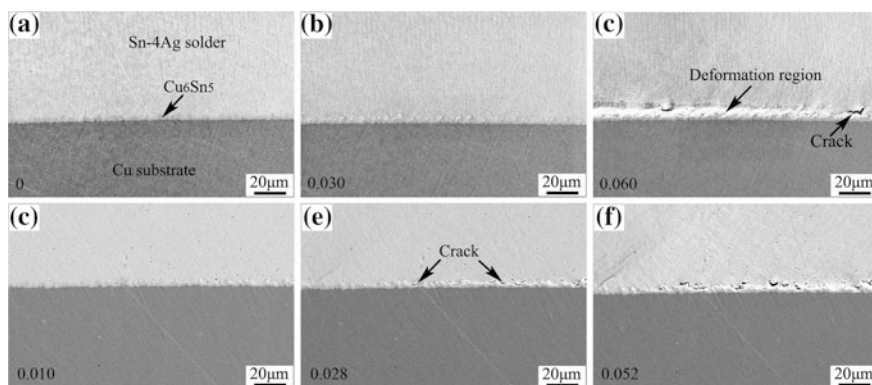


**Fig. 2.14** Interfacial fracture morphologies of Sn-4Ag/Cu solder joints reflowed for 3 min and tested at the strain rate of **a–c**  $3.3 \times 10^{-3} \text{ s}^{-1}$  and **d–f**  $1.33 \times 10^{-2} \text{ s}^{-1}$ . Reprinted from Ref. [19]. Copyright 2012, with permission from AIP Publishing LLC



tested at the strain rate of  $3.3 \times 10^{-3} \text{ s}^{-1}$ . As in Fig. 2.14a, b, obvious deformation mismatch between the solder and the  $\text{Cu}_6\text{Sn}_5$  layer occurs shortly after the tensile test. At higher strain, deformation of the solder close to the joints interface becomes serious, and some microcracks appear inside the solder, as in Fig. 2.14c. Compared with the solder joints reflowed for 1 min, the strain concentration zone is a bit wider, and there is also no fracture in the  $\text{Cu}_6\text{Sn}_5$  layer. Figure 2.14d–f show the fracture process of the solder joints tested at the strain rate of  $1.33 \times 10^{-2} \text{ s}^{-1}$ . As in the figures, deformation of the solder also increases with increasing strain, and the step induced by the deformation mismatch is more obvious, but the plastic deformation is less serious since the yield strength of the solder is higher at higher strain rate. Besides, some  $\text{Cu}_6\text{Sn}_5$  grains fractured during the tensile process, indicating that they are more apt to fracture at higher strain rate.

Figure 2.15 shows the interfacial fracture process of the solder joints reflowed for 8 min and tested at the strain rate of  $1.1 \times 10^{-3} \text{ s}^{-1}$ . Before the tensile test, the side surface of the sample is very flat, as in Fig. 2.15a. At the strain of 0.02, deformation mismatch started to emerge at interface (see Fig. 2.15b). In Fig. 2.15c, d, some  $\text{Cu}_6\text{Sn}_5$  grains have fractured, although plastic deformation of the solder is not very serious. During the latter deforming process, the cracks in the  $\text{Cu}_6\text{Sn}_5$  grains propagated into the solder and connected with each other, inducing the fracture along the joint interface, as in Fig. 2.15e, f. According to Figs. 2.13, 2.14, and 2.15, it can be concluded that there are always deformation mismatch and strain concentration inside the solder around the  $\text{Cu}_6\text{Sn}_5$ /solder interface. The solder joints always fracture around the joint interface, but the exact fracture location is a little bit different and affected by the reflow times and tensile strain rate. The solder joints reflowed for a long time or deformed at higher strain rate are more apt to fracture inside the IMC layer.

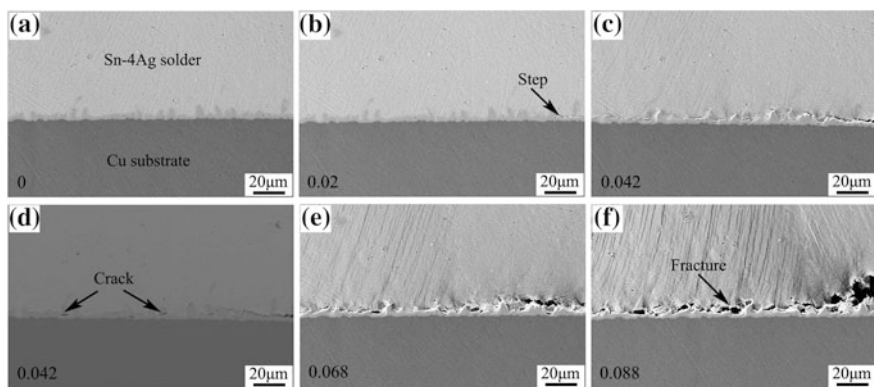


**Fig. 2.15** Interfacial fracture morphologies of Sn-4Ag/Cu solder joints reflowed for 8 min and tested at the strain rate of  $1.1 \times 10^{-3} \text{ s}^{-1}$ . Reprinted from Ref. [19]. Copyright 2012, with permission from AIP Publishing LLC

### 2.4.3 Applied Stress and Fracture Behavior of Cu<sub>6</sub>Sn<sub>5</sub> Grains

To further reveal the fracture behaviors of the Cu<sub>6</sub>Sn<sub>5</sub> grains, the stress applied on them are quantitatively analyzed. As the stress endured by the Cu<sub>6</sub>Sn<sub>5</sub> grain is applied by the solder, the shear stress is calculated through dividing the shear force with the underside area of the grain, and the shear force is obtained by multiplying the stress of the solder with the projection area of the hood face of the Cu<sub>6</sub>Sn<sub>5</sub> grain. Since the shape of the grain is described by the revolving body of the parabola  $y = a \cdot x^2$ , the force endured by the Cu<sub>6</sub>Sn<sub>5</sub> grain is calculated by the follow equation:

$$F = 2\tau_{\text{solder}} \int_0^{r^2} 2xdy = 4\tau_{\text{solder}} \int_0^r xdx^2 = a\tau_{\text{solder}} \frac{8}{3}r^3 \quad (2.1)$$

and the stress is calculated to be:

$$\tau_{\text{IMC}} = F / \pi r^2 = \frac{8a\tau_{\text{solder}}r^3}{3\pi r^2} = 0.849ar\tau_{\text{solder}} \quad (2.2)$$

where  $F$  is the shear force,  $\tau_{\text{solder}}$  is the stress in the solder close to the Cu<sub>6</sub>Sn<sub>5</sub>/solder interface which envelops Cu<sub>6</sub>Sn<sub>5</sub> grain, and  $\tau_{\text{IMC}}$  is the shear stress at the foundation of the Cu<sub>6</sub>Sn<sub>5</sub> grain; the size  $r$  is a dimensionless number in this equation.

Based on Eq. (2.2) and the shape of the Cu<sub>6</sub>Sn<sub>5</sub> grains exhibited in Sect. 2.4.1, the stresses endured by the protrudent Cu<sub>6</sub>Sn<sub>5</sub> grains at the joint interfaces reflowed for different times were calculated and are shown Fig. 2.16. It can be found that  $\tau_{\text{IMC}}$  increases obviously with increasing reflow time. For the interface reflowed for 8 min, the shear stress on the protrudent Cu<sub>6</sub>Sn<sub>5</sub> grains is 2.836 times as large as that in the solder. The von Mises stress distribution inside the solder joint has also revealed that the stress at the corner of the solder is about twice as high as the stress in the solder joint [13]. Since the tensile stress in this study is about 70 MPa, the shear stress on the protrudent Cu<sub>6</sub>Sn<sub>5</sub> grains was estimated to be about 300–400 MPa, which is close to their fracture stress under shear loading and bending moment [18]. Therefore, the protrudent Cu<sub>6</sub>Sn<sub>5</sub> grains at these interfaces usually fracture during the tensile or shear process [29]. In contrast, both the shear stress and the bending moment on the small Cu<sub>6</sub>Sn<sub>5</sub> grains are much lower, thus they can hardly fracture prior to fracture of the solder.

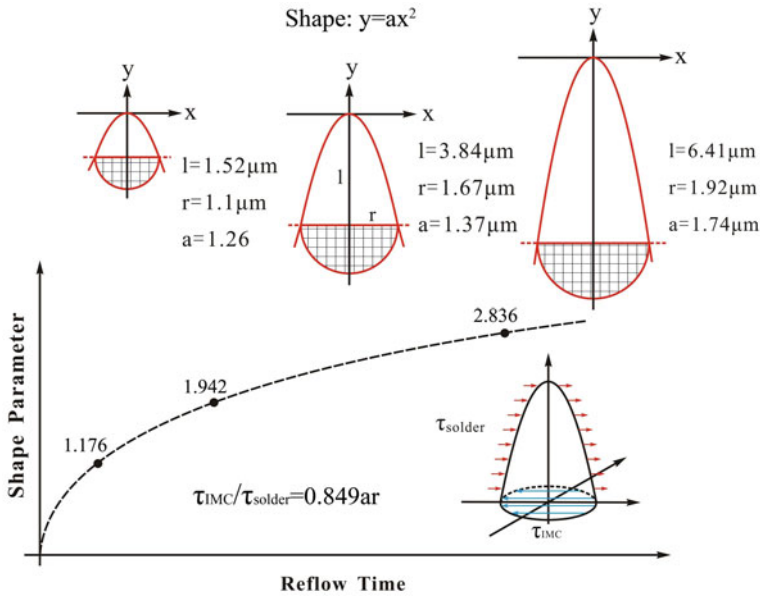


**Fig. 2.16** Analysis diagram of the shear stress applied on the  $\text{Cu}_6\text{Sn}_5$  grains reflowed for different times. Reprinted from Ref. [19]. Copyright 2012, with permission from AIP Publishing LLC

## 2.5 Fracture Behavior of Cu–Sn IMCs Induced by Deformation of Substrate

### 2.5.1 Morphology of IMCs at Sn–4Ag/Cu Interface

The morphologies of the IMC layers at the as-soldered and aged Sn–4Ag/Cu interfaces were observed and are shown in Fig. 2.17. Figure 2.17a presents the morphology of the as-soldered Sn–4Ag/Cu single crystal interface, in which the IMC thickness is about 2  $\mu\text{m}$ , and Energy Dispersive X-ray Detector (EDX) analysis indicates that it is  $\text{Cu}_6\text{Sn}_5$ . After aging for 4 days, the IMC thickness increases to about 7  $\mu\text{m}$ , as in Fig. 2.17b, and a fuscous IMC layer appears between the Cu and  $\text{Cu}_6\text{Sn}_5$  layer, which was confirmed to be  $\text{Cu}_3\text{Sn}$  by EDX. The morphologies of the Sn–Ag/cold-drawn Cu interfaces are a little bit different from that of the Sn–Ag/Cu single crystal interfaces. As in Fig. 2.17c, the IMC layer at the as-soldered Sn–Ag/cold-drawn Cu interface is a little thicker, and some protrudent  $\text{Cu}_6\text{Sn}_5$  grains were observed. That may attribute to the difference in microstructure of the Cu substrates, because the growth rates of the IMC grains at different crystallographic planes of the Cu crystal are different [24, 25]. Since the cold-drawn Cu is composed of thin crystal grains with different orientations, the  $\text{Cu}_6\text{Sn}_5$  grains at different grains are different in growth rate, making some of them become protrudent. After aging for 4 days, the IMC layer becomes much thicker,

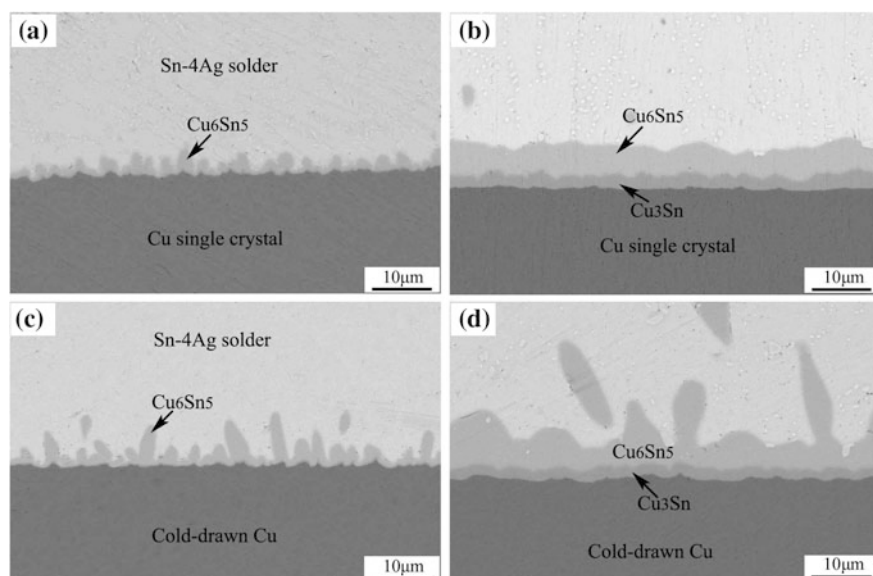
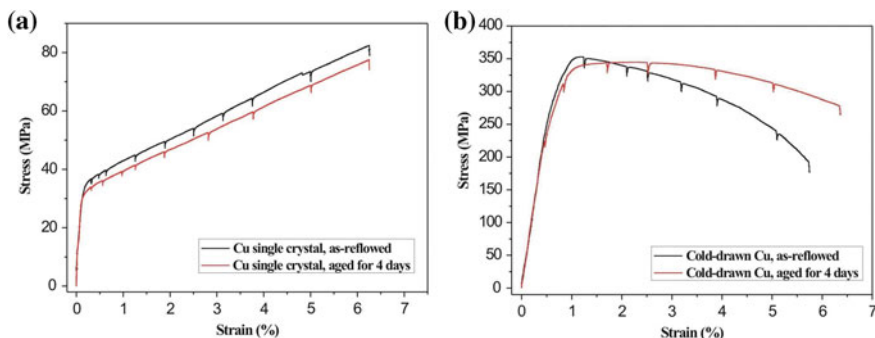


**Fig. 2.17** Interfacial morphologies of Sn–4Ag/Cu single crystal solder joints **a** as-reflowed and **b** aged for 4 days; Sn–4Ag/cold-drawn Cu solder joints **c** as-reflowed and **d** aged for 4 days. Reprinted from Ref. [20]. Copyright 2011, with permission from Elsevier

and some protrudent  $\text{Cu}_6\text{Sn}_5$  grains still exist (see Fig. 2.17d). In general, the IMC layers at the Sn–Ag/cold-drawn Cu interface are a little thicker and coarser than that at the Sn–4Ag/Cu single crystal interface.

### 2.5.2 Fracture Behavior of Interfacial IMC Layer

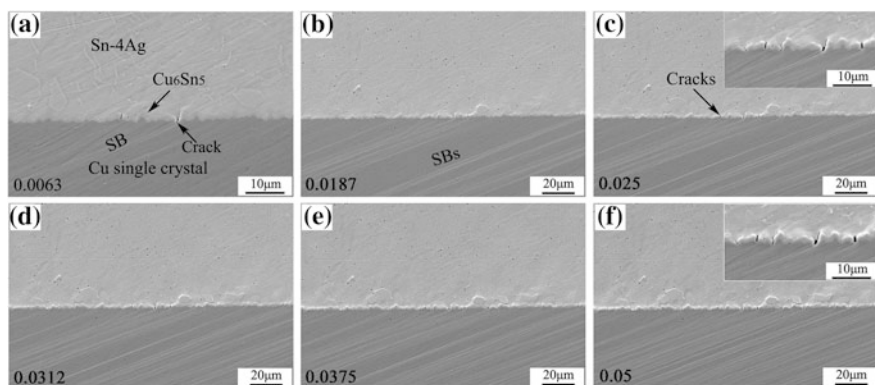
The tensile stress–strain curves of the two groups of Sn–Ag/Cu specimens are shown in Fig. 2.18. As the IMC layers are very thin and the solder is very soft, the curves can be approximately regarded as the tensile curves of the Cu substrates. Figure 2.18a shows the stress–strain curves of the Sn–4Ag/Cu single crystal sample, it can be seen that the yield strength is about 32 MPa, and there is a long strain hardening stage after yielding. Even when the strain has exceeded 6 %, the specimen shows no necking or fracture. In contrast, the yield strength of the cold-drawn Cu is much higher, while the strain hardening stage is very short. As in Fig. 2.18b, the yield strength of the cold-drawn Cu is about 300 MPa and the yield strain is about 1 %, and necking occurs shortly after yielding. When the tests were paused at certain strains, the stress shows slight decrease, which was induced by stress relaxation. The aged Sn–Ag/cold-drawn Cu sample exhibits a lower yield strength but better ductility because recovery occurs during the aging process. In contrast, since there are few defects in the Cu single crystal, the thermal aging has



**Fig. 2.18** Nominal stress–strain curves of samples: **a** Sn–Ag/Cu single crystal samples, **b** Sn–Ag/cold-drawn Cu samples. Reprinted from Ref. [20]. Copyright 2011, with permission from Elsevier

little influence on it, and the difference in their yield strength was predicated to be induced by their different Schmidt factors. The deformation behavior of the Cu substrates is dominative on fracture behaviors of the interfacial IMC layers, which will be shown later in detail.

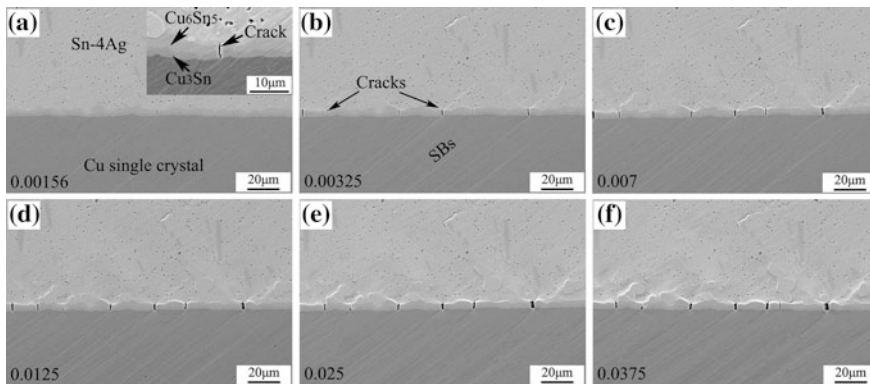
The fracture morphologies of the IMC layer ( $\text{Cu}_6\text{Sn}_5$ ) at the as-soldered Sn–Ag/Cu single crystal interface are shown in Fig. 2.19, and the strains are tagged in each figure. Figure 2.19a exhibits the interfacial morphology at a strain of  $6.3 \times 10^{-3}$ , in which obvious slip bands (SBs) have appeared and a few cracks inside the IMC layer are visible. In comparison, the thin  $\text{Cu}_6\text{Sn}_5$  layer in the as-soldered tensile solder joints can hardly fracture [13, 26]. Besides, there is clear correspondence between the cracks and the slip bands, which is similar to the Sn–Ag–Cu/Cu interface deformed under fatigue loadings [30]. However, there is no fracture in the IMC layer before the slip bands emerge and act on the IMC/Cu



**Fig. 2.19** Fracture behaviors of as-soldered Sn–Ag/Cu single crystal interfaces at different strains: **a**  $\epsilon = 6.3 \times 10^{-3}$ , **b**  $\epsilon = 1.87 \times 10^{-2}$ , **c**  $\epsilon = 2.5 \times 10^{-2}$ , **d**  $\epsilon = 3.12 \times 10^{-2}$ , **e**  $\epsilon = 3.75 \times 10^{-2}$ , **f**  $\epsilon = 5 \times 10^{-2}$ . Reprinted from Ref. [20]. Copyright 2011, with permission from Elsevier

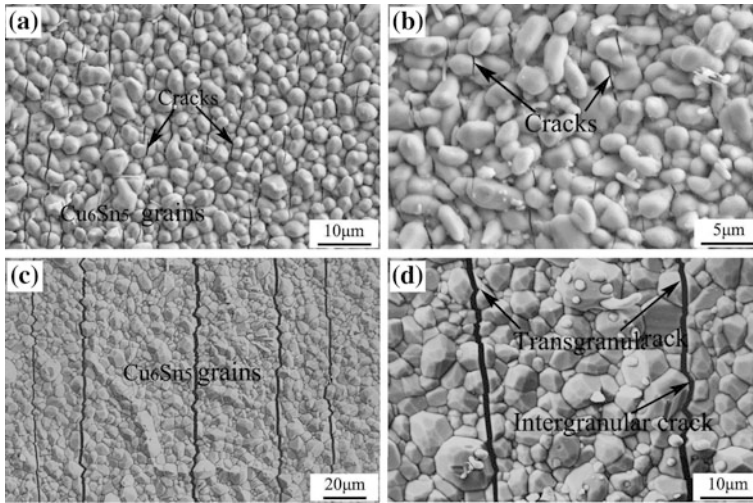
interface. With increasing strain, the slip bands become more and more serious, as in Fig. 2.19b, c, and the width and number of the cracks increase obviously. In the latter deforming process, only the width of the cracks keeps increasing, while their number shows little increase (see Fig. 2.19d–f). According to the correspondence between the slip bands and the cracks in the IMC layer, it is deduced that the cracks may be induced by impingement of the slip bands in the Cu substrate.

Figure 2.20 shows the fracture morphologies of the IMC layer ( $\text{Cu}_6\text{Sn}_5 + \text{Cu}_3\text{Sn}$ ) at the Sn–Ag/Cu single crystal interface aged for 4 days, and the strains are also tagged in each figure. In Fig. 2.20a, the strain is only  $1.56 \times 10^{-3}$ , but a few thin cracks have been observed in the IMC layer. However, there is also no cracking in the IMC layer before the slip bands act on the IMC/Cu interface. In Fig. 2.20b, c, both the number and the width of the cracks increase obviously, and the corresponding relationship between the slip bands and the cracks is more obvious. Although the  $\text{Cu}_6\text{Sn}_5$  and  $\text{Cu}_3\text{Sn}$  layers are a little bit different in mechanical properties [5], the vertical cracks can easily propagate from the  $\text{Cu}_3\text{Sn}$  into  $\text{Cu}_6\text{Sn}_5$ , because the  $\text{Cu}_6\text{Sn}_5$  and  $\text{Cu}_3\text{Sn}$  are hard and brittle and are closely bonded. In contrast, the cracks cannot get through the  $\text{Cu}_6\text{Sn}_5$ /solder interface. In Fig. 2.20d–f, the evolution of the cracks is similar to that in Fig. 2.19, i.e., the width of the cracks increases obviously but no further increase in the number. Generally, the fracture behaviors of the IMC layer in Figs. 2.19 and 2.20 are quite different from that in the solder joint under tensile or shear loading [13, 26, 31]. There is no strain concentration inside the solder close to the joint interface, and the cracks are vertical to the joint interface. In fact, since the Cu substrate is the carrier, the deformation of the IMC layer is driven by the substrate, and then the solder is driven to deform by the IMC layer. Therefore, the solder can deform freely and no restraint stress is applied on the IMC layer to make it fracture. Considering the correspondence between the slip bands and the vertical cracks, it is concluded that it is the impingement of the slip bands (dislocations) that induces the fracture in the IMC layer.



**Fig. 2.20** Fracture behaviors of aged Sn–Ag/Cu single crystal interfaces at different strains: **a**  $\varepsilon = 1.56 \times 10^{-3}$ , **b**  $\varepsilon = 3.25 \times 10^{-3}$ , **c**  $\varepsilon = 7 \times 10^{-3}$ , **d**  $\varepsilon = 1.25 \times 10^{-2}$ , **e**  $\varepsilon = 2.5 \times 10^{-2}$ , **f**  $\varepsilon = 3.75 \times 10^{-2}$ . Reprinted from Ref. [20]. Copyright 2011, with permission from Elsevier





**Fig. 2.21** Fracture morphologies of IMC grains at Sn–Ag/Cu single crystal interfaces: **a** and **b** as-reflowed samples; **c** and **d** samples aged for 4 days. Reprinted from Ref. [20]. Copyright 2011, with permission from Elsevier

The morphologies of the IMC grains at the Sn–Ag/Cu single crystal interfaces after the tests are shown in Fig. 2.21, in which the loading direction is indicated by the arrows. The observed IMCs are Cu<sub>6</sub>Sn<sub>5</sub> grains as the Cu<sub>3</sub>Sn is covered by them. Figure 2.21a, b presents the morphologies of the as-soldered Cu<sub>6</sub>Sn<sub>5</sub> grains; it was found that the grains are not very compact and their grain size is about a few microns. The cracks are similar in direction, and both transgranular and intergranular cracks appear. The Cu<sub>6</sub>Sn<sub>5</sub> grains at the aged interfaces are much larger, compact, and equiaxed, and the cracks are more regular. As in Fig. 2.21c, the cracks are straight and parallel with each other. Because the cracks are induced by the slip bands, they have similar distribution with the latter, and the widths are different as they fracture at different time. At higher magnification, the transgranular fracture is found to be the major fracture mechanisms, although fracture may also occur along the grain boundaries when the slip bands are close to them (see Fig. 2.21d). Compared with the cracks in the as-soldered IMC layer, the cracks in the aged IMC layer are much wider but their density is lower, which is well consistent with the interfacial fracture morphologies in Figs. 2.19 and 2.20.

The fracture behaviors of the IMC layers at the Sn–Ag/cold-drawn Cu interfaces are a little bit different from that at the Sn–Ag/Cu single crystal interfaces, as shown in Figs. 2.22 and 2.23. Figure 2.22a presents the morphology of the as-soldered Sn–Ag/cold-drawn Cu interface at a strain of  $1.24 \times 10^{-2}$ , in which the sample just started to yield, some slip bands appeared at the surface of the Cu substrate and a few cracks in the IMC layer (pure Cu<sub>6</sub>Sn<sub>5</sub>) are visible. Compared with the as-reflowed Sn–Ag/Cu single crystal interface, the critical “fracture strain” of the



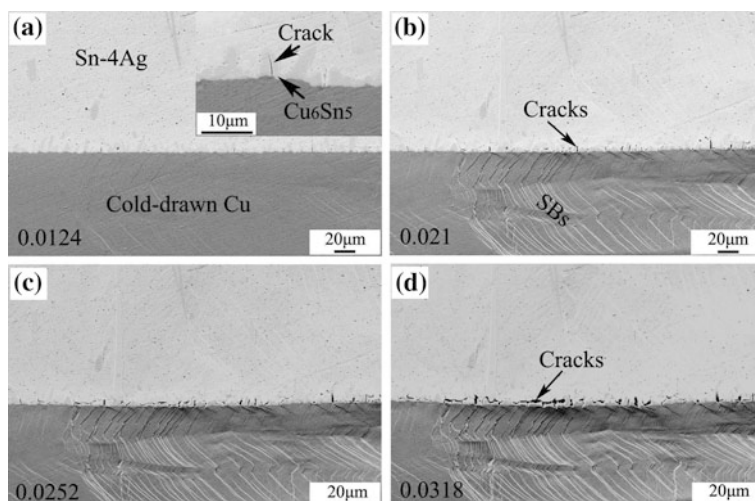


**Fig. 2.22** Fracture behaviors of as-reflowed Sn–Ag/cold-drawn Cu interfaces at different strain: **a**  $\varepsilon = 1.24 \times 10^{-2}$ , **b**  $\varepsilon = 2.1 \times 10^{-2}$ , **c**  $\varepsilon = 2.52 \times 10^{-2}$ , **d**  $\varepsilon = 3.18 \times 10^{-2}$ . Reprinted from Ref. [20]. Copyright 2011, with permission from Elsevier

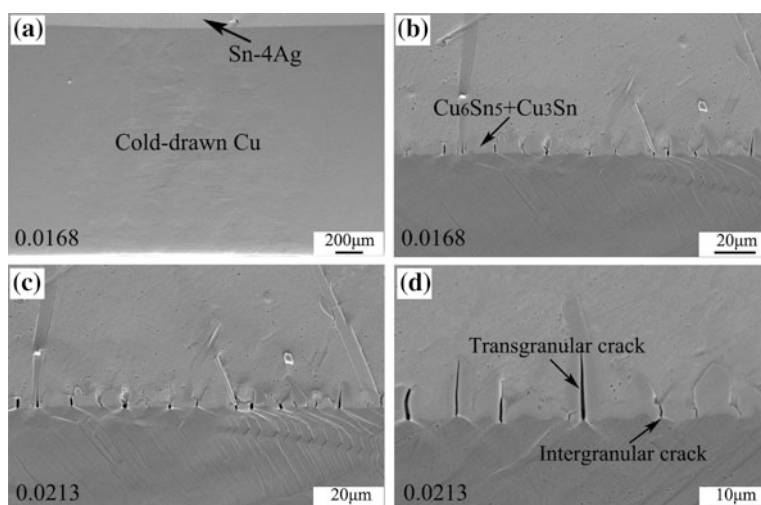


**Fig. 2.23** Fracture behaviors of aged Sn–Ag/cold-drawn Cu interfaces: **a** macroscopic deformation and **b** microscopic fracture morphologies of joint interface at the strain of  $1.68 \times 10^{-2}$ ; **c** and **d** fracture morphologies of joint interface at the strain of  $2.13 \times 10^{-2}$ . Reprinted from Ref. [20]. Copyright 2011, with permission from Elsevier

IMC layer (the strain for occurrence of the fracture in the IMC layer) is much higher. However, there is also no fracture in the IMC layer before the Cu substrate yields. The necking of the cold-drawn Cu sample occurs shortly after the yielding

and generates a serious strain concentration. At higher magnification, some cracks are found to be very sharp, indicating that they initiate at the IMC/Cu interface and propagate to the IMC/solder interface. Figure 2.22b shows the necking region of the specimen at a strain of  $2.1 \times 10^{-2}$ , the cracks in the IMC layer are serious, and there is also clear correspondence between the cracks and the slip bands. Whereas, the plastic deformation of the Cu substrate beyond the necking region is not obvious, and there is no cracking in the IMC layer. During the further deforming process, the cracks become wider, gradually turn to the solder/IMC interface and connect with each other to form long cracks (see Fig. 2.22c, d). That phenomenon does not appear in Figs. 2.19 and 2.20 because the deformation of Cu substrates is not so serious. Due to the serious strain concentration, deformation and fracture at the necking region develop very fast.

The fracture behaviors of the IMC layer ( $\text{Cu}_6\text{Sn}_5 + \text{Cu}_3\text{Sn}$ ) at the aged Sn–Ag/cold-drawn Cu interface are similar to that at the as-reflowed interface, and the critical “fracture strain” of the IMC layer is about  $1.1 \times 10^{-2}$ , as exhibited in Fig. 2.23. Figure 2.23a shows the macroscopic deformation morphology at a strain of  $1.68 \times 10^{-2}$ , it is notable that the plastic deformation is obvious at the necking region, but slight at the other region. In microscale, the cracks were only observed at the necking region, and there is also clear correlation between the slip bands and the vertical cracks, as in Fig. 2.23b. Compared with that shown in Fig. 2.20, the plastic deformation is complex and the slip bands are different in orientation, making the cracks in the IMC layer a bit random. In Fig. 2.23c, d, the slip bands and the cracks become wider but their number changes little, both the intergranular and the transgranular cracks can be observed at higher magnification, and some sharp cracks are obvious. In general, the IMC layers in Figs. 2.22 and 2.23 fracture at high stress/strain, but that only occurs at the necking region, and there is also correspondence between the slip bands and the cracks in the IMC layers.

The morphologies of the cracked IMC grains at the Sn–Ag/cold-drawn Cu interfaces are shown in Fig. 2.24, the loading direction is also indicated by the arrows. Figure 2.24a, b display the  $\text{Cu}_6\text{Sn}_5$  grains at the as-reflowed interface. The cracks are approximately parallel and vertical to the loading direction, and can be either intergranular or transgranular. Although the two figures are taken from the same sample, the widths of the cracks are quite different since the plastic strains at different locations are different. The  $\text{Cu}_6\text{Sn}_5$  grains at the aged interface are larger and equiaxed, and the intergranular and the transgranular cracks are clearer, as in Fig. 2.24c, d. Besides, the cracks are not exactly parallel with each other and the intergranular cracks are more common, because the cold-drawn Cu is composed of thin grains with different orientations and accordingly random slip bands, making the cracks in the IMC layer less regular.

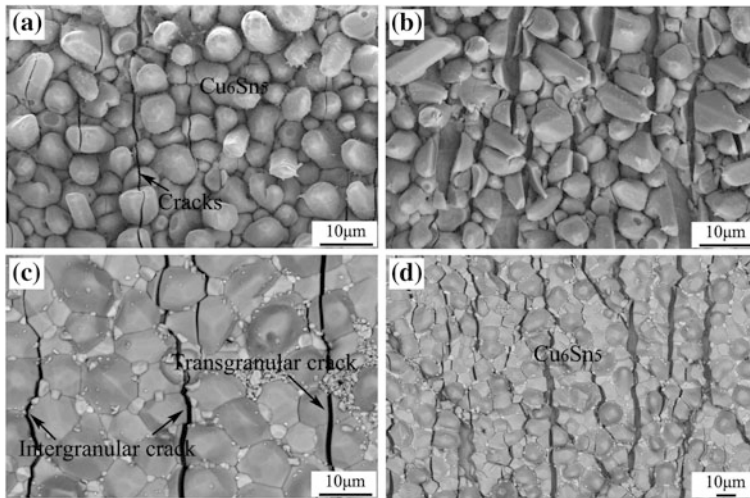


**Fig. 2.24** Fracture morphologies of IMC grains at Sn–4Ag/cold-drawn Cu interfaces: **a** and **b** as-reflowed samples; **c** and **d** samples aged for 4 days. Reprinted from Ref. [20]. Copyright 2011, with permission from Elsevier

### 2.5.3 Fracture Mechanisms Induced by Deformation of Substrate

According to the observations above, there is definite correspondence between the slip bands and the cracks in the IMC layers. Besides, the fracture process of the IMC layer is similar to the transition of plastic deformation between the metallic grains. In the polycrystalline metals, the slip systems of the grains with preferential orientations are stimulated firstly and the dislocations in these grains slip outwards to the grain boundary [32, 33]. As the dislocations cannot get across the larger angle grain boundaries, they pile-up at the boundaries and induce a cumulative stress ahead the pile-up group [32, 34]. When the number of the piled dislocations increases to a critical value, the cumulative stress will stimulate the slip system in the adjacent grain [35, 36], or sometimes induces a microcrack [32]. As the fracture in the IMC layer occurs when the dislocations impinge on it, it may be also induced by the piled dislocations. It has been well accepted that the  $\text{Cu}_6\text{Sn}_5$  has two structural forms, i.e. the conventional NiAs-type structure ( $\eta$ ) and the ordered long-period superlattice structure (LPS) based on the NiAs-type structure ( $\eta'$ ) [3, 37], and  $\text{Cu}_3\text{Sn}$  has a long-period superstructure ( $\epsilon$ ) [38], both of them are essentially different from the face-centered cubic Cu substrates in lattice structure. Therefore, the dislocations in the Cu substrates cannot get across the  $\text{Cu}_6\text{Sn}_5/\text{Cu}$  or  $\text{Cu}_3\text{Sn}/\text{Cu}$  interfaces, and it is probable for them to pile-up at the two interfaces and induces the fracture.

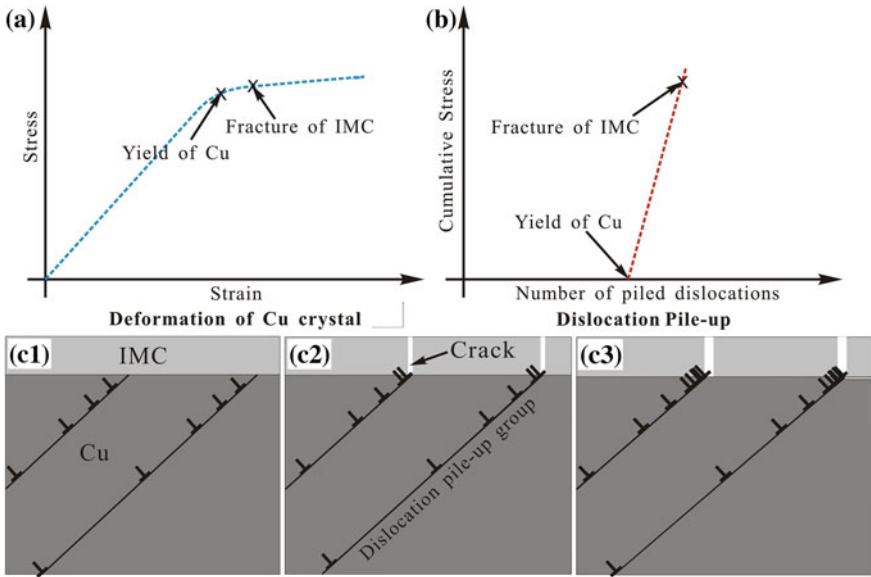


**Fig. 2.25** Illustration on fracture of interfacial IMC layer induced by dislocation pile-up: **a** sketch deformation curve of a Cu crystal grain; **b** relationship between cumulative stress and piled dislocations; **c1–c3** dislocation pile-up at the interface and fracture processes of the IMC. Reprinted from Ref. [20]. Copyright 2011, with permission from Elsevier

A qualitative illustration on the fracture behaviors of the IMC layer based on the dislocation pile-up mechanism is exhibited in Fig. 2.25. Figure 2.25a shows a sketch deformation curve of a Cu grain at the IMC/Cu interface. At the beginning of the deformation process, the Cu grain deforms elastically and no fracture occurs in the IMC layer. After the Cu yields, the dislocations in the Cu grain are stimulated to slip. If there is no barrier, they will emerge at the surface and form some slip steps. However, as they cannot get across the IMC/Cu interface, they have to pile-up at the interface and induce a cumulative stress field ahead of the piled-up dislocations, as shown in Fig. 2.25c1. With increasing strain, the dislocation sources in the Cu grain keep giving out dislocations, and the number of the piled dislocations and the cumulative stress increase gradually (see Fig. 2.25b). When the cumulative stress reaches the fracture strength of the IMC layer, microscale fracture occurs in the  $\text{Cu}_6\text{Sn}_5$  or  $\text{Cu}_3\text{Sn}$  at the IMC/Cu interface. Since the IMCs are hard and brittle [13, 24], the microcracks propagate rapidly, forming the cracks vertical to the tensile direction, as in Fig. 2.25c2. In the latter process, the dislocations at the cracks increase continually with increasing strain, making the slip bands and the cracks become wider (see Fig. 2.25c3). As the fracture of the IMC layer is induced by the dislocation pile-up, yielding of the Cu substrates is a necessary condition of that.

Since the IMC/Cu interface is only at one side of the Sn–Ag/Cu specimen, the dislocation pile-up at the IMC/Cu interface is single-side style. For the single-side

dislocation pile-up, the number of dislocations in the piled-up group and the cumulative stress can be estimated by the following equations [39]:

$$n = \pi(1 - \nu)L\tau/Gb \quad (2.3)$$

$$\tau_h = n\tau \quad (2.4)$$

where  $b$  is Burgers vector,  $L$  is the length of the dislocation pile-up groups, which approximates to the grain size of the Cu substrate,  $\nu$  is the Poisson ratio,  $G$  is the shear modulus,  $\tau$  is the shear component of the tensile stress and  $\tau_h$  is the cumulative stress on the obstacle (equal to the stress applied on the first dislocation in the pile-up group). For the Cu crystal,  $b$  is  $1.81 \times 10^{-10}$  m,  $\nu$  is 0.343 and  $G$  is 48 GPa. In Fig. 2.20, the orientation of the loading direction was determined to be around [11 20 24], accordingly the stimulated slip system is  $(\bar{1} \ 1 \ 1)$  [1 0 1] and the Schmidt factor is calculated to be 0.430. As the IMC layer fractures at 32 MPa,  $\tau$  is calculated to be 13.76 MPa. The length of the dislocation pile-up group ( $L$ ) is obtained to be 4 mm through dividing the width of the specimen with the cosine of the angle between the loading direction and slip direction. Based on that,  $n$  is calculated to be  $1.31 \times 10^4$  and  $\tau_h$  is 179.8 GPa in theory. However, as the hardness of Cu<sub>6</sub>Sn<sub>5</sub> is about 3 GPa and its compression strength is about 1.4 GPa [11, 13], the cumulative stress can not really achieve the foreside value, because a much smaller number of piled dislocations will make the IMC layer fracture to release the cumulative stress. For the cold-drawn Cu,  $L$  is around 50–100  $\mu\text{m}$ , while the shear stress ( $\tau$ ) is much higher, and the theoretical cumulative stress has the same order of magnitude with that at the Sn–Ag/Cu single crystal interface. Since the cumulative stress of a small group of dislocations is very high, it will soon reach the fracture strength of IMC layer after the dislocations arrive at the Cu/IMC interface, thus the IMC layers at both the two Sn–Ag/Cu interfaces fracture very shortly after yielding of the Cu substrates.

As exhibited before, the critical “fracture strain” of the IMC layer at the Sn–Ag/cold-drawn Cu interface is higher than 1 %. As its elastic modulus is about 180 GPa [13], the IMC layer should endure a stress higher than 1.8 GPa if it is continuous, which is even higher than its compressive strength [11]. Therefore, the IMC layer may not be a continuous, and the fracture proposed above are not the only mechanism to accommodate the deformation. There may be some gaps between the IMC grains that can be opened under tensile stress. To confirm that, a thin sheet was sliced from the undeformed as-soldered Sn–Ag/cold-drawn Cu joint, and ground manually to a few microns. Figure 2.26 shows its morphologies observed by SEM. As in the figure, there are thin gaps between the Cu<sub>6</sub>Sn<sub>5</sub> grains, and most of them extend to the Cu substrate. Though the sample may undergo a slight plastic deformation when it was ground, there are no slip bands or transgranular fracture in the IMC layer, thus the openings can only be induced by the surface deformation, which provides direct evidence for the predication on the gaps and openings. After the aging process, the gaps may still exist, at least the IMC grain boundaries are weak links, because the IMC layer in Fig. 2.23 also fractures at

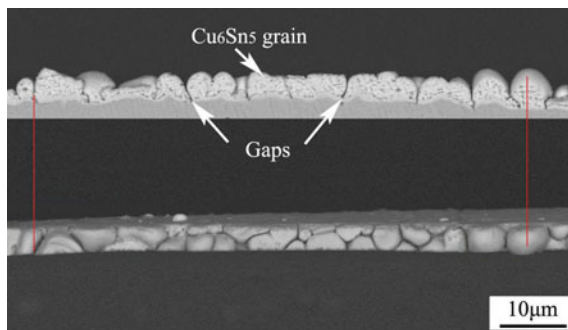


**Fig. 2.26** Gaps between the  $\text{Cu}_6\text{Sn}_5$  grains at the as-reflowed Sn–4Ag/cold-drawn Cu interface, the lines indicate the correspondence between the cross-section and the side section views. Reprinted from Ref. [20]. Copyright 2011, with permission from Elsevier

a strain higher than 1 %. There should also be such gaps between the  $\text{Cu}_6\text{Sn}_5$  grains at the Sn–Ag/Cu single crystal interface, but the opening is less preferred because the IMC layer fractures at a low strain. The difference between the openings and the intergranular cracks is that the latter is wider and induced by dislocation pile-up. The openings are predicated to be the major mechanisms to release the surface deformation and elastic deformation, but they are not obvious and will not sharply decrease the adhesive properties of the joint interface.

The qualitative illustrations on the fracture behaviors of the IMC layers at the two Sn–Ag/Cu interfaces are shown in Fig. 2.27, with the slip bands represented by the broken lines. For the Sn–Ag/Cu single crystal interface, the fracture behavior is simple, as shown in Fig. 2.27a. After the Cu substrate yields, the dislocations slip and pile-up at the IMC/Cu interface, leading to the fracture in the IMC layer shortly after that. The cracks can be transgranular or intergranular, depending on the location of the slip bands. Similar to the distribution of the slip bands in the Cu single crystal, they are also exactly parallel to each other. Besides, there are also thin openings between the IMC grains. Figure 2.27b shows the fracture behaviors at the Sn–Ag/cold-drawn Cu interface. As the cold-drawn Cu is polycrystalline composed of grains with the size 50–100  $\mu\text{m}$  and each of them has different orientations, fracture behaviors of the IMC layer are a bit complex. According to the Hall–Petch relationship, the metals with thinner grains have higher yield strength because fewer dislocations piled-up at the grain boundaries at the same stress [40]. Therefore, the slip bands in the cold-drawn Cu and the cracks in the IMC layer are thinner compared with the coarse grains. Besides, since yielding of the Cu substrate is a necessary condition for fracture in the IMC layer, the critical fracture strain of the IMC layer at the Sn–Ag/cold-drawn Cu interface is much higher, and the cracks are a bit in disorder due to the complex slip bands in the cold-drawn Cu grains. There are also both intergranular and transgranular cracks, and the intergranular cracks are more common because the slip bands are denser and have higher possibility to appear at the IMC grain boundaries. In addition, the



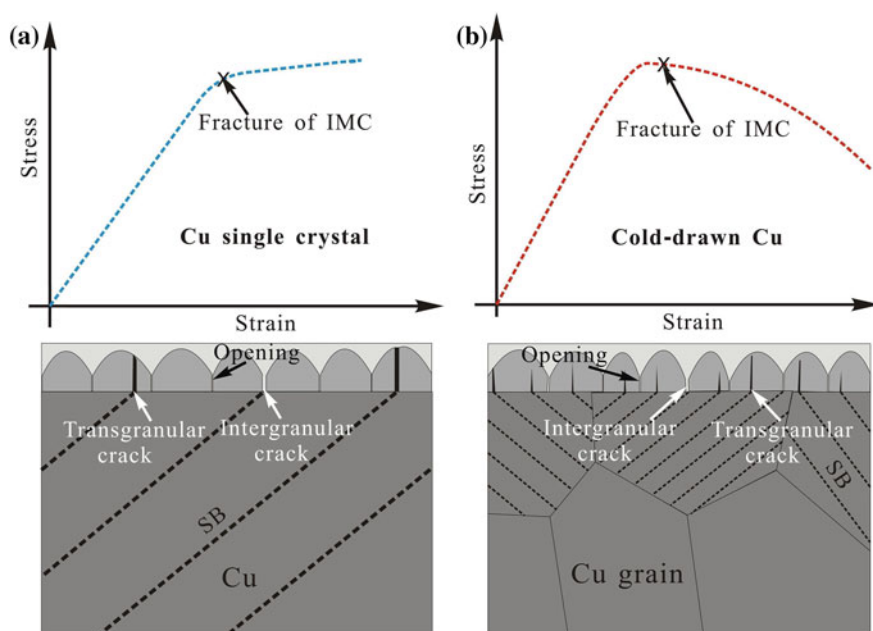


**Fig. 2.27** Illustration on fracture behaviors of IMC layers at **a** Sn–Ag/Cu single crystal sample and **b** Sn–Ag/cold-drawn Cu sample. Reprinted from Ref. [20]. Copyright 2011, with permission from Elsevier

openings between the IMC grains are more serious as the surface deformation of Cu substrate is much higher.

Based on the understandings on the fracture mechanisms, some intrinsic and extrinsic factors can affect the fracture of IMC layer induced by deformation of the Cu substrate. As the IMC layer fractures when the piled-up dislocations act on it, it is very sensitive to plastic deformation of the Cu substrate. Therefore, the yield strength/strain of the Cu substrate has dominative influence on fracture behavior of the IMC layer. Because the yield strength of the Cu substrate relies mainly on its grain size, the latter can dominate the fracture behaviors of the interfacial IMC layer. The IMC layer at the Cu substrates with thin grains fractures at a high stress/strain, while that at the coarse-grained substrate fractures at a low stress. Besides, as the fracture of the IMC layer at the necking region is much more serious, it is expected that a strain concentration in the Cu substrate can induce a serious local strain, making the fracture of the IMC layer at that region more serious.

Compared with their sensitivity to the plastic deformation, the IMC layers can withstand a very high elastic deformation. According to Figs. 2.22 and 2.23, even when the strain increases to 1 %, no cracking occurs inside the IMC layer if no slip band emerges in the Cu substrate, because the gaps between the IMC grains can accommodate the elastic strain. The thermal aging has significant influence on



fracture behaviors of the IMC layer as its fracture strength decreases after thermal aging [41], making it easier to fracture. Moreover, the IMC grains become much more compacted after the aging process, and the opening at the grain boundaries not so easy to occur, thus the intergranular cracking will be more favored.

## 2.6 Brief Summary

In this chapter, fracture behavior of the IMC layer at the Sn–4Ag/Cu solder joint interface were investigated. The shear fracture behavior and fracture strength of the  $\text{Cu}_6\text{Sn}_5$  grain was studied using Dynamic Ultramicroscopic Hardness tester, the fracture behavior of IMC layer induced by deformation of solder and Cu substrate were in situ observed, the influencing factors on the fracture behavior were discussed. The major conclusions are as follows:

- (1) Cleavage fracture occurs in the  $\text{Cu}_6\text{Sn}_5$  grains when the shear stress applied on it increase to a certain value, result in a burst increase of strain on the indentation curves. The  $\text{Cu}_6\text{Sn}_5$  grains usually fracture at the foundation or the center portion, depending on their size and shape. The slender  $\text{Cu}_6\text{Sn}_5$  grains are more likely to fracture at the foundation at a lower stress, induced by shear stress and the flexural torque, while the podgy grains tend to fracture at the center portion, result from the shear stress. The fracture strength of the  $\text{Cu}_6\text{Sn}_5$  grains fractured at their center portion is close to the shear strength of the  $\text{Cu}_6\text{Sn}_5$  IMC, which is about 670 MPa.
- (2) The thickness and surface roughness of the interfacial  $\text{Cu}_6\text{Sn}_5$  layer at the Sn–4Ag/Cu joint interfaces increase linearly with increasing square root of the reflow time, some protrudent  $\text{Cu}_6\text{Sn}_5$  grains appear at the joint interface after reflowed for a long time, and their shapes can be approximately described by the revolution body of parabola. Serious strain concentration occurs around the joint interface during the tensile process, the joint interfaces reflowed for longer time usually fractures in the  $\text{Cu}_6\text{Sn}_5$  layer. For the joint interface reflowed for 8 min, the shear stress applied on the protrudent  $\text{Cu}_6\text{Sn}_5$  grains by solder is calculated to be about 300–400 MPa. At high strain rate, the stress applied on the  $\text{Cu}_6\text{Sn}_5$  by the solder is higher which makes the IMC layer easier to fracture.
- (3) The IMC layers at the Sn–Ag/Cu single crystal interfaces and Sn–Ag/cold-drawn Cu interfaces fracture shortly after the yield of the Cu substrate, forms the cracks vertical to the joint interface which correlate well with the slip bands in the Cu substrates. In microscale, the fracture is induced by dislocation pile-up. After the Cu substrates yield, the dislocations pile-up at the IMC/Cu interface and generate a high cumulative stress ahead the pile-up group. Fractures inside the IMC layer occur when the cumulative stress reaches the fracture strength of the IMC. As a small group of piled dislocations can induce a very high cumulative stress, fracture of the IMC

layer occurs very shortly after the Cu substrates yield. Plastic deformation of the Cu substrates can be regarded as the sufficient condition for fracture of the IMC layer, and the grain size of the Cu substrate has dominative influence on the fracture behaviors. Thermal aging makes the IMC layers thicker, more compact, and easier to fracture. There are thin gaps between the IMC grains that can be opened under tensile stress to accommodate the surface deformation, thus the IMC layer can withstand a large elastic strain before the yield of the Cu substrate.

## References

1. Chan YC, Yang D. Failure mechanisms of solder interconnects under current stressing in advanced electronic packages. *Prog Mater Sci.* 2010;55:428–75.
2. Prakash KH, Sritharan T. Interface reaction between copper and molten tin-lead solders. *Acta Mater.* 2001;49:2481–9.
3. Laurila T, Vuorinen V, Kivilahti JK. Interfacial reactions between lead-free solders and common base materials. *Mater Sci Eng R.* 2005;49:1–60.
4. Dao M, Chollacoop N, Van Vliet KJ, Venkatesh TA, Suresh S. Computational modeling of the forward and reverse problems in instrumented sharp indentation. *Acta Mater.* 2001;49:3899–918.
5. Deng X, Chawla N, Chawla KK, Koopman M. Deformation behavior of (Cu, Ag)–Sn intermetallics by nanoindentation. *Acta Mater.* 2004;52:4291–303.
6. He M, Chen Z, Qi GJ. Solid state interfacial reaction of Sn–37Pb and Sn–3.5Ag solders with Ni–P under bump metallization. *Acta Mater.* 2004;52:2047–56.
7. Chromik RR, Vinci RP, Allen SL, Notis MR. Nanoindentation measurements on Cu–Sn and Ag–Sn intermetallics formed in Pb-free solder joints. *J Mater Res.* 2003;18:2251–61.
8. Ghosh G. Elastic properties, hardness, and indentation fracture toughness of intermetallics relevant to electronic packaging. *J Mater Res.* 2004;19:1439–54.
9. Jang GY, Lee JW, Duh JG. The nanoindentation characteristics of  $\text{Cu}_6\text{Sn}_5$ ,  $\text{Cu}_3\text{Sn}$ , and  $\text{Ni}_3\text{Sn}_4$  intermetallic compounds in the solder bump. *J Electron Mater.* 2004;33:1103–10.
10. Yang PF, Lai YS, Jian SR, Chen J, Chen RS. Nanoindentation identifications of mechanical properties of  $\text{Cu}_6\text{Sn}_5$ ,  $\text{Cu}_3\text{Sn}$ , and  $\text{Ni}_3\text{Sn}_4$  intermetallic compounds derived by diffusion couples. *Mater Sci Eng A.* 2008;485:305–10.
11. Jiang L, Chawla N. Mechanical properties of  $\text{Cu}_6\text{Sn}_5$  intermetallic by micropillar compression testing. *Scripta Mater.* 2010;63:480–3.
12. Kikuchi S, Nishimura M, Suetsugu K, Ikari T, Matsushige K. Strength of bonding interface in lead-free Sn alloy solders. *Mater Sci Eng A.* 2001;319–321:475–9.
13. Lee HT, Chen MH, Jao HM, Liao TL. Influence of interfacial intermetallic compound on fracture behavior of solder joints. *Mater Sci Eng A.* 2003;358:134–41.
14. Kima KS, Huh SH, Sukanuma K. Effects of intermetallic compounds on properties of Sn–Ag–Cu lead-free soldered joints. *J Alloys Compd.* 2003;352:226–36.
15. Zou HF, Zhang ZF. Ductile-to-brittle transition induced by increasing strain rate in Sn–3Cu/Cu joints. *J Mater Res.* 2008;23:1614–7.
16. Hu GJ, Goh KY, Judy L. Micromechanical analysis of copper trace in printed circuit boards. *Microelectron Reliab.* 2011;51:416–424.
17. Sinkovics B, Krammer O. Board level investigation of BGA solder joint deformation strength. *Microelectron Reliab.* 2009;49:573–8.

18. Zhang QK, Tan J, Zhang ZF. Fracture behaviors and strength of Cu<sub>6</sub>Sn<sub>5</sub> intermetallic compounds by indentation testing. *J Appl Phys*. 2011;110:014502.
19. Zhang QK, Zhang ZF. Influences of reflow time and strain rate on interfacial fracture behaviors of Sn–4Ag/Cu solder joints. *J Appl Phys*. 2012;112:064508.
20. Zhang QK, Zhang ZF. In-situ observations on fracture behaviors of Cu–Sn IMC layers induced by deformation of Cu substrates. *Mater Sci Eng A*. 2011;530:452–61.
21. Yoon JW, Kim SW, Jung SB. Interfacial reaction and mechanical properties of eutectic Sn–0.7Cu/Ni BGA solder joints during isothermal long-term aging. *J Alloys Compd*. 2005;391:82–9.
22. Kim SW, Yoon JW, Jung SB. Interfacial reactions and shear strengths between Sn–Ag–based Pb-Free Solder Balls and Au/EN/Cu Metallization. *J Electron Mater*. 2004;33:1182–9.
23. Kerr M, Chawla N. Creep deformation behavior of Sn–3.5Ag solder/Cu couple at small length scales. *Acta Mater*. 2004;52:4527–35.
24. Shang PJ, Liu ZQ, Pang XY, Li DX, Shang JK. Growth mechanisms of Cu<sub>3</sub>Sn on polycrystalline and single crystalline Cu substrates. *Acta Mater*. 2009;57:4697–706.
25. Zou HF, Yang HJ, Zhang ZF. Morphologies, orientation relationships and evolution of Cu<sub>6</sub>Sn<sub>5</sub> grains formed between molten Sn and Cu single crystals. *Acta Mater*. 2008;56:2649–62.
26. Zhang QK, Zhang ZF. Fracture mechanism and strength-influencing factors of Cu/Sn–4Ag solder joints aged for different times. *J Alloy Compd*. 2009;485:853–61.
27. Lang F, Tanaka H, Munegata O, Taguchi T, Narita T. The effect of strain rate and temperature on the tensile properties of Sn–3.5Ag solder. *Mater Charact*. 2005;54:223–9.
28. Bai N, Chen X, Fang Z. Effect of strain rate and temperature on the tensile properties of tin-based lead-free solder alloys. *J Electron Mater*. 2008;37:1012–9.
29. Date M, Shoji T, Fujiyoshi M, Sato K, Tu KN. Ductile-to-brittle transition in Sn–Zn solder joints measured by impact test. *Script Mater*. 2004;51:641–5.
30. Zhu QS, Zhang ZF, Shang JK, Wang ZG. Fatigue damage mechanisms of copper single crystal/Sn–Ag–Cu interfaces. *Mater Sci Eng A*. 2006;435–436:588–94.
31. Yao P, Liu P, Liu J. Effects of multiple reflows on intermetallic morphology and shear strength of SnAgCu–xNi composite solder joints on electrolytic Ni/Au metallized substrate. *J Alloys Compd*. 2008;462:73–9.
32. Zhang ZF, Wang ZG. Grain boundary effects on cyclic deformation and fatigue damage. *Prog Mater Sci*. 2008;53:1025–99.
33. Kumar KS, Van Swygenhoven H, Suresh S. Mechanical behavior of nanocrystalline metals and alloys. *Acta Mater*. 2003;51:5743–74.
34. Zhang ZF, Wang ZG. Dependence of intergranular fatigue cracking on the interactions of persistent slip bands with grain boundaries. *Acta Mater*. 2003;51:347–64.
35. Meyers MA, Mishra A, Benson DJ. Mechanical properties of nanocrystalline materials. *Prog Mater Sci*. 2006;51:427–556.
36. Head AK. Dislocation group-dynamics. 6. Release of a pile-up. *Philos Mag*. 1973;27:531–539.
37. Larsson AK, Stenberg L, Lidin S. The superstructure of domain-twinned  $\eta'$ —Cu<sub>6</sub>Sn<sub>5</sub>. *Acta Crystall B*. 1994;50:636–43.
38. Kao C. Microstructures developed in solid-liquid reactions: using Cu–Sn reaction, Ni–Bi reaction, and Cu–In reaction as examples. *Mater Sci Eng A*. 1997;238:196–201.
39. Cottrell AH. Dislocations and plastic flow in crystals. London: Oxford University Press; 1953.
40. Armstrong R, Codd I, Douthwaite RM, Petch NJ. The plastic deformation of polycrystalline aggregates. *Philos Mag*. 1962;7:45–58.
41. Zeng K, Tu KN. Six cases of reliability study of Pb-free solder joints in electronic packaging technology. *Mater Sci Eng R*. 2002;38:55–105.

Investigations on Microstructure and Mechanical  
Properties of the Cu/Pb-free Solder Joint Interfaces

Zhang, Q.

2016, XV, 143 p. 115 illus., 81 illus. in color., Hardcover

ISBN: 978-3-662-48821-8